The mechanism of kinesin inhibition by kinesin binding protein

Joseph Atherton[1, 2*], Jessica J. A. Hummel[3], Natacha Olieric[4], Julia Locke[2,5], Alejandro Peña[2,6], Steven S. Rosenfeld[7], Michel O. Steinmetz[4,8], Casper C. Hoogenraad[3] and Carolyn A. Moores[2]

[1] Randall Centre for Cell and Molecular Biophysics, King's College, London, United Kingdom.

[2] Institute of Structural and Molecular Biology, Birkbeck, University of London, London, United Kingdom.

[3] Cell Biology, Neurobiology and Biophysics, Department of Biology, Faculty of Science, Utrecht University, Utrecht, the Netherlands.

[4] Laboratory of Biomolecular Research, Division of Biology and Chemistry, Paul Scherrer Institut, Villigen PSI, Switzerland.

[5] Current address: Macromolecular Machines Laboratory, The Francis Crick Institute, London, United Kingdom.

[6] Current address: Department of In Silico Drug Discovery, Pharmidex Pharmaceuticals, Hatfield, United Kingdom.

[7] Department of Cancer Biology, Mayo Clinic, Jacksonville, FL, USA.

[8] University of Basel, Biozentrum, CH-4056 Basel, Switzerland

* corresponding author: joseph.atherton@kcl.ac.uk

Abstract

Subcellular compartmentalisation is necessary for eukaryotic cell function. Spatial and temporal regulation of kinesin activity is essential for building these local environments via control of intracellular cargo distribution. Kinesin binding protein (KBP) interacts with a subset of kinesins via their motor domains, inhibits their microtubule (MT) attachment and blocks their cellular function. However, its mechanisms of inhibition and selectivity have been unclear. Here we use cryo-electron microscopy to reveal the structure of KBP and of a KBP-kinesin motor domain complex. KBP is a TPR-containing, right-handed α-solenoid that sequesters the kinesin motor domain's tubulin-binding surface, structurally distorting the motor domain and sterically blocking its MT attachment. KBP uses its α-solenoid concave face and edge loops to bind the kinesin motor domain, and selected structure-guided mutations disrupt KBP inhibition of kinesin transport in cells. The KBP-interacting motor domain surface contains motifs exclusively conserved in KBP-interacting kinesins, suggesting a basis for kinesin selectivity.

Introduction

Kinesins are a superfamily of microtubule (MT)-based molecular motors that play important roles in cellular functions such as mitosis, cell motility and intracellular transport[1-3]. Kinesins are categorised into 14 sub-classes (kinesin-1 to kinesin-14[4]) by motor domain conservation and within these sub-classes individual family members (a total of 45 'KIF' or 'Kif' genes in humans and mice respectively) have a wide range of functional characteristics and biological roles[1,5]. Dysfunction of kinesin family members has been implicated in a number of pathological conditions[6,7]. The kinesin motor domain is the microtubule-binding engine that drives these activities, converting the chemical energy of ATP binding and hydrolysis into mechanical force. While these mechanical forces are classically used to generate motility in transport kinesins, some kinesin family members drive MT organisation or depolymerisation of MTs.

Kinesins are highly regulated in order to prevent both waste of ATP and to spatially and temporally control kinesin function. This is particularly important in highly polarised and compartmentalised cells such as neurons. Kinesin regulation via inhibition of their motor domains can occur through a number of mechanisms that limit ATPase activity and/or block track binding - these include intramolecular inhibition by kinesin tail domains, post-translational modification of the motor, or through interactions with regulatory binding partners. Recently, it has been demonstrated that a subset of kinesin superfamily members, including kinesin-2s, -3s, -8s and -12s, are sequestered by kinesin binding protein (KBP; KIF1BP; KIAA1279), which inhibits MT track attachment by their motor domains and, thus, blocks their MT-related functions[8-10].

KBP is expressed in multiple human tissues including brain and heart[8]. Mutations in the KBP have been identified as causing autosomal recessive Goldberg-Shprintzen syndrome (GOSHS)[11-14], which presents as congenital facial dysmorphia, nervous system pathology and dysfunction and heart defects[15]. In addition, KBP gene copy number has been recently reported as predictive in paediatric neuroblastoma prognosis, prompting its suggestion as a drug target[16]. KBP was originally identified as a kinesin-3 binding partner that modulated its mitochondrial transport function[8]; however, KBP has since been shown to interact with a subset of other kinesin family members to regulate diverse cellular processes including mitosis[17,18], spermatogenesis[19] and neuronal differentiation, growth and cargo distribution[10,20-24].

We do not currently know what the structure of KBP is, nor understand the mechanism of KBP-kinesin inhibition. It is also completely unknown how KBP differentiates between particular kinesin family members. KBP is a 72 kDa protein, is predicted to contain several tetratricopeptide repeats (TPRs) and to be mainly α-helical in secondary structure content[8,9]. Here we present cryo-electron microscopy (cryo-EM) structures of KBP alone and of KBP bound to the motor domain of the human mitotic kinesin KIF15 (a 110 kDa complex). We show that KBP is a TPR-containing, right-handed α-solenoid protein composed of 9 antiparallel α-helix pairs interrupted by a linker region. We also show that KBP's concave face binds KIF15 via its MT-binding elements and induces a large displacement of the kinesin α4 helix, sterically inhibiting MT association. Finally, we show that KBPs kinesin selectivity is associated with specific kinesin sequences spread across the interaction surface.

Results

KBP is a TPR-containing, right-handed α-solenoid

The 3D structure of the ~72 kDa KBP at 4.6 Å resolution (Figure 1 and Figure 1–figure supplement 1a,b) was determined using cryo-EM data collected using a Volta Phase Plate (VPP), and an atomic model was calculated (see Methods). Our structure revealed that KBP is a right-handed α-solenoid protein (Figure 1a,b and Figure 1–figure supplement 1c-e). Nine pairs of anti-parallel α-helices (αHP1 (α-helical pair 1) to αHP9) are broken by a single 'linker α-helix' (LαH) and 'linker loop' (LL) in the centre of the fold separating KBP into N-terminal and C-terminal subdomains (Figure 1 and Figure 1–figure supplement 1c-e, Figure 1–figure supplement 2). The four predicted TPR motifs contribute exclusively to α-helical pairs in the N-terminal subdomain (Figure 1a,d,e).

The supercoiling α-helical pairs form concave and convex faces linked by short and long loops that constitute the two edges of the α-solenoid (Figure 1–figure supplement 1c-e, Figure 1–figure supplement 2). In contrast to the shorter loops, the longer loops (>7 residues) tend to be partially disordered, show low sequence homology between KBP orthologues in different species and are mainly found in the N-terminal subdomain (e.g. L2, L6 and L10, Figure 1–figure supplement 1d-e, Figure 1–figure supplement 2). The linker loop is the longest (62 residues) and is thus unique in the KBP structure because it is reasonably conserved and mainly ordered, with visible corresponding density clearly bridging the N and C-terminal subdomains (Figure 1a-b, Figure 1–figure supplement 1d-e, Figure 1–figure supplement 2 and Figure 1–figure supplement 3). Despite this clear ordered density, this loop was not

modelled due to low homology to available structures and a lack of consensus in secondary structure prediction (see Methods). In spite of this lack of consensus, density in this region suggests that part of this loop may form further α-helical structures. Other TPR-containing α-solenoid proteins form important regulatory interactions in numerous contexts, and the structure we describe is indicative of similar properties for KBP.

KBP conformationally adapts to bind KIF15's motor domain using both subdomains

To elucidate the mechanism of kinesin inhibition by KBP, we determined the structure of KBP in complex with the human KIF15 (kinesin-12) motor domain (KIF15_MD, 1-375). This construct, which has six of its eight cysteine residues mutated to serine (C5S, C50S, C162S, C294S, C314S, C346S) and two additional cysteines were inserted (S250C, G375C), has comparable steady state ATPase activity to previously published reports[25] (Figure 2–figure supplement 1a) and we refer to it as KIF15_MD6S. The overall resolution of this KBP-KIF15_MD6S complex was 6.9 Å, with KBP and KIF15_MD6S determined to similar local resolutions (Figure 2–figure supplement 1b-c). We built a model of the complex via flexible fitting using our KBP model and the KIF15_MD crystal structure (Figure 2a,b and see Methods). The complex is arranged such that KIF15_MD6S sits in the concave face of the KBP α-solenoid, analogous to a baseball enclosed in a baseball glove. The kinesin MD is positioned centrally between the N and C-terminal subdomains and contacts the KBP concave face and loops at the α-solenoid edges.

When the structure of KBP-alone is superimposed onto KBP in the KBP-KIF15_MD6S complex, it is clear that KBP undergoes a conformational change in the presence of its kinesin motor domain binding partner, with the largest differences resulting from an unfurling motion of its N-terminal subdomain (Figure 2c,d and Video 1). The KBP-alone model is incompatible with KIF15_MD6S binding, due to clashes with L14 in the C-terminal subdomain and αHP3a, αHP4a and L8 in the N-terminal subdomain. The conformational changes in KBP upon KIF15_MD6S binding relieves these clashes in the complex (Video 1).

To establish whether the KBP-KIF15_MD6S mode of interaction applied to other kinesins, we also collected data of the complex formed by KBP with the motor domain of the human kinesin-3 KIF1A (KIF1A_MD). 2D classification of these images revealed a number of classes with an extra-density corresponding the size of a kinesin motor domain bound to the concave face of KBP, consistent with what was observed in the KBP-KIF15_MD6S dataset (Figure 2–figure supplement 1c). However, in contrast to the KBP-KIF15_MD6S sample, these KBP-KIF1A_MD 2D classes provided only limited views of the complex (Figure 2–figure supplement 1c,d), such that a reliable 3D structure could not be calculated. Intriguingly, in addition, the extra kinesin density in the 2D classes appeared to have a somewhat flexible position relative to KBP. However, these data did allow us to confirm that indeed KIF1A_MD also interacts with KBP on its concave face in the same way as KIF15_MD6S and suggests a common mechanism of kinesin inhibition by KBP.

KIF15_MD6S binds KBP via rearrangement of its tubulin-binding subdomain

We examined the effect of KBP binding on the conformation of KIF15_MD6S. Kinesin motor domains can be structurally divided into three distinct subdomains[26,27] which undergo coordinated conformational changes during the MT-based kinesin ATPase cycle. MT binding stabilises the tubulin-binding subdomain of the MD while the P-loop and Switch 1/2 subdomains – which contain the conserved nucleotide-coordinating P-loop and Switch 1 and 2 motifs - move relative to each other in response to the nucleotide state of the MD[26-28]. We determined the structure of the MT-bound, AMPPNP state of KIF15_MD6S, which shows that this MD adopts a canonical conformation (Figure 3–figure supplement 1). Comparison of this conformation with an ADP-bound Kif15_MD crystal structure (PDB: 4BN2[25]) illustrates the scale of these MT- and nucleotide-dependent subdomain rearrangements in KIF15, which are similar to those seen in other kinesins MDs[26,28,29] (Figure 3–figure supplement 1d,e and Figure 3c,d).

The structure of the KBP-KIF15_MD6S complex revealed that KBP binds the kinesin motor domain via the tubulin-binding subdomain (Figure 3). While the P-loop and Switch 1/2 subdomains of the KIF15_MD crystal structure and associated Mg^{2+}-ADP generally fitted well into density of the KBP-KIF15_MD6S complex, a large portion of the tubulin-binding subdomain did not (Figure 3a; Figure 3–figure supplement 2a,b). In particular, there is a striking lack of density in the expected position for helix α4 (Figure 3a; Figure 3–figure supplement 2b). Instead, there was strong density of length and width consistent with helix α4 displaced by ~15 Å into the concave face of KBP, and which we modelled as such (Figure 3b,e, Figure 2 and Figure 3–figure supplement 2b-e). This displacement of helix α4, which lies close to the TPR-repeat region of the N-terminal subdomain of KBP, is accompanied by additional rearrangements of the flanking L11 and L12 in KIF15_MD6S (labelled

KL11 and KL12, Figure 3c-e: Figure 3–figure supplement 2b-e). A number of other TPR-containing α-solenoids are known to bind peptide motifs with α-helical content within their concave faces[30-32] (Figure 3–figure supplement 3), and our structure shows that KBP binds helix α4 of KIF15_MD6S in a similar way.

The KBP-bound conformation of the KIF15_MD6S tubulin-binding subdomain is also radically different from its MT-bound conformation (Figure 3d-e). The tubulin-binding subdomain forms the majority of the MT-binding surface in the KIF15_MD6S-MT complex (Figure 3d, Figure 3–figure supplement 1) such that KBP and MTs cannot simultaneously bind KIF15_MD6S due to extensive steric overlap (Figure 3d-e). In summary, KBP sequesters and blocks the MT-interacting surface of kinesin motor domains via a mechanism that involves significant conformational change within the motor domain.

KBP binds kinesin motor domains via conserved motifs in the α-solenoid edge loops and α-helices at the concave face

KBP contacts the KIF15_MD6S both via 1) loops connecting the α-solenoid edges and 2) TPR-containing α-helices at the concave face (Figure 4, Figure 4–figure supplement 1 and Video 2). At the α-solenoid edges, L1, L3, L5 and L10 in the N-terminal subdomain and L12, L14, L16 and L18 in the C-terminal subdomain are close enough to KIF15_MD6S to be involved in binding. The closest interaction of these were KBP L12 and L14, which contact both Kβ5-KL8 and KL12-Kα5-KL13 regions of the KIF15 tubulin-binding subdomain (Figure 4). KBP's disordered L1 lies close to KIF15_MD6S's KL9, while the shorter, ordered L3 and L5 are situated near but not contacting KL11 and Kα6 (Figure 4–figure supplement 1a,b). KBP's C-

terminal L16 and L18 are close enough to KIF15_MD6S that they may interact with the flexible KL12, N-terminus or neck-linker. At the TPR-containing region of the concave face of KBP, αHP4a, αHP4b and αHP5a contact the K11-Kα4-KL12 region of KIF15_MD6S (Figure 4c-d).

To test the functional significance of this interface, we investigated KBP-kinesin interactions in cells, and examined the activities of mutant KBP constructs in which the predicted interacting amino acids within potentially kinesin-contacting loops were substituted for Ala, Gly or Pro residues (Figure 1–figure supplement 2, and Table 2). Ala-substitutions in the TPR-containing α-helices at the KBP concave face were also introduced at particularly inter-species conserved polar residues predicted to interact with the KIF15_MD K11-Kα4-KL12 region (Tyr-213 and Gln-216 in αHP4a, Gln-238 in αHP4b, Thr-255 and Gln-258 in αHP5a; Figure 4c,d and Figure 1–figure supplement 2). All mutant constructs exhibited roughly equivalent expression patterns which were also comparable to WT KBP (Figure 5 – figure supplement 1).

We first used pull-down assays. Mouse Kif15 or Kif1A constructs consisting of only the motor domain and the first coiled-coil region (Kif15_MDC or Kif1A_MDC) were fused to bioGFP and co-expressed with various HA-tagged human KBP constructs in HEK293T cells, followed by pull-down of HA-KBP by the bioGFP-KIF_MDC[9] (Figure 5–figure supplement 2). Although there are moderate qualitative differences in binding by the two motors, the effects of KBP mutations on motor binding – described in following - are essentially the same. Ala-substitutions in the TPR-containing α-helices at the KBP concave face (αHP4a, αHP4b), which lie at the heart of the KBP- KIF15_MD6S structural interface, strongly reduced KBP's interaction with both KIF15_MDC and KIF1A_MDC. αHP5a mutants had a similar

but less pronounced effect (Figure 5–figure supplement 2b,c). In contrast, mutation of L1, L3 or L5 in the KBP N-terminal subdomain or L10 or L16 in the C-terminal subdomain – none of which form directly visualised interactions with KIF15_MD6S in the cryo-EM reconstruction - has no effect on KBP's interaction with either KIF15_MDC or KIF1A_MDC (Figure 5–figure supplement 2b,c). Mutation of L12 (to some extent) and of L14 (to a greater extent) – which contact both Kβ5-KL8 and KL12-Kα5-KL13 - reduced KBP interaction with KIF15_MDC and KIF1A_MDC (Figure 5–figure supplement 2 b,c). Mutation of L12 + L14 additively disrupted the KBP-motor interaction, consistent with the structural proximity of these two loops in the kinesin-KBP complex. L10 + L12 and L10 + L14 mutants also had weaker interactions with KIF15_MDC/KIF1A_MDC (Figure 5–figure supplement 2 b,c), again pointing to the additive contributions of loops in the KBP C-terminal subdomain to kinesin binding. Strikingly, mutation of L18 appears to enhance the interaction between KBP and both KIF15_MDC and KIF1A_MDC, suggesting that it may somehow contribute to negative regulation of binding in the context of WT KBP.

We then used a previously described inducible peroxisome translocation assay in COS-7 cells[9]. In this assay, dimeric mouse Kif15_MDC or Kif1A_MDC constructs with an FRB-tag (Kif15_MDC-FRB or Kif1A_MDC-FRB) are expressed together with PEX-mRFP-FKBP, a peroxisome-binding construct, along with the various KBP constructs. Addition of rapalog induces FRB-FKBP heterodimerisation and motor-driven peroxisome translocation to the cell periphery, but when the motor is inhibited by KBP, peroxisome translocation is blocked (Figure 5a-c). Kinesin-mediated translocation was measured, first by quantifying the number of cells in which peroxisome translocation is seen (Figure 5 d, e), and second, by quantifying peroxisome intensities above a threshold value in the cell periphery (Figure 5 f, g).

Because of observed differences in peroxisome translocation within the time-frame of rapalog treatment, different peroxisome intensity threshold values and peripheral areas were used for KIF1A and KIF15; this is probably due to differences in motor properties (Figure 5 – figure supplement 3).

Intriguingly, while the overall trends in perturbation of KBP inhibition by mutagenesis seen in the pulldown assay are recapitulated in the translocation assay, some differences are also observed. As with the pull-down assay, Ala-substitutions in the TPR-containing α-helices αHP4a and αHP4b at the KBP concave face, as well as αHP5a, all strongly reduced KBP's inhibition of both KIF15_MDC and KIF1A_MDC peroxisome translocation activity (Figure 5d-g). This can be seen by the extent of peroxisome translocation and in an increase of peroxisomes in the cell periphery after rapalog addition, similar to the control condition without KBP (Figure 5d-g). Also, as observed in the pull-down assay, mutation of L1, L3 or L5 had no effect on KBP's inhibition of KIF15_MDC or KIF1A_MDC (Figure 5d-g). This reinforces the conclusion that while these elements are close enough to form contacts with the parts of the kinesin motor domain in our reconstruction, they do not contribute significantly to KBP inhibition of kinesin-mediated translocation in cells.

Mutation of either of L12 or L14 strongly abrogated KBP inhibition of KIF15_MDC/KIF1A_MDC-based translocation, a more pronounced effect than was seen in the pull-down assay. Similarly, although mutation of L10 and L16 had no effect on KBP-kinesin interaction in the pull-down assay, mutation of these loops disrupted KBP inhibition of KIF1A_MDC and KIF15_MDC in the translocation assay (Figure 5d-g). A subset of the above described mutations were also combined to assess additive effects. Here we observed that KBP constructs containing mutations in both L10 + L12, L10 + L14 or L12 + L14 had similar effects to KBP with only one of

290 the loops mutated (Figure 5d-g), suggesting that KBP inhibition is more readily
291 disrupted in the translocation assay.
292 Interestingly, while all the above described regions affected KBP inhibition of
293 KIF15_MDC and KIF1A_MDC equivalently, the L18 KBP mutant inhibited
294 KIF15_MDC equivalent to wild type, but only exhibited partial inhibition of
295 KIF1A_MDC-mediated translocation. It should, however, be noted that fewer cells
296 show peroxisome translocation by KIF1A_MDC when L18 is co-expressed (Figure
297 5e), suggesting that the L18 KBP mutant also inhibits KIF1A_MDC to some extent.
298 The L18 mutant is the single example of contradictory behaviours between the assays,
299 because it appeared to enhance KBP-kinesin binding in the pull-down assay. Our
300 structural data do not provide a clear rationale for this, and future studies will
301 investigate the role of this region of KBP further and, for example, whether it is
302 subject to post-translational regulation that could regulate KBP's inhibitory activity.
303 However, taken together, the translocation and pull-down assays both
304 demonstrate the functional importance of the kinesin interaction with the TPR-
305 containing α-helices at the KBP concave face and the set of loops in the KBP C-
306 terminal subdomain. The translocation and pull-down assays also reveal differences in
307 the sensitivity of the KBP-kinesin interaction to perturbation, where translocation is
308 more readily disrupted than the interactions detected by pull-down. These differences
309 likely reflect the greater complexity of motor regulation during active translocation
310 and could be a function of FRB-FKBP-mediated motor dimerization. It might also
311 reflect the fact that cellular MTs in the translocation assay can directly compete with
312 KBP for kinesin binding. Overall, these mutation studies support the idea that KBP
313 interacts with different kinesin family members in a similar way via an extended

interface at KBP's concave face that is composed of TPR-containing α-helices and α-solenoid edge loops, particularly in the C-terminal subdomain.

Specific sequences in the tubulin-binding subdomain are conserved across KBP-binding kinesin family members

Given that KBP selectively binds and inhibits only a subset of kinesins[9], we used our structural data to investigate the basis of this selectivity. Although the resolution of our reconstruction and the flexibility of some loops do not provide a detailed molecular description of the interaction interface, our structure shows that the kinesin tubulin-binding subdomain is the key KBP-interacting region. Analysis of the sequences of this region in KBP-binding and KBP-non-binding kinesins (Figure 6a) revealed patterns of sequence conservation across the entire subdomain in all KBP-binding kinesins; this included both the Kβ5-KL8 and KL11-Kα4-KL12-Kα5-KL13 regions. In contrast, the equivalent regions are more variable in kinesins that are not inhibited by KBP. The length of KL8, which joins the two Kβ5 strands, was also consistently 5 residues long in KBP-binding kinesins, while it was variable in KBP-non-binding kinesins. From our KBP- KIF15_MD6S structure, the sensitivity of the KBP interaction to KL8 length makes sense considering the tight fit of this loop between KBP L12 and L14 (Figure 6b). In summary, two consensus motifs in KL11-Kα4-KL12-Kα5-KL13 and Kβ5-KL8 regions of the tubulin-binding subdomain are found in KBP-binding kinesins and these are likely to form the basis of KBP's kinesin family member selectivity. We therefore propose a model where KBP selects and inhibits target kinesins through binding and remodelling a compatible tubulin-binding subdomain, obstructing the kinesin MT-binding surface (Figure 6c).

Discussion

In this study, we reveal the TPR-containing right-handed α-solenoid structure of the ~72 kDa KBP using VPP cryo-EM. At the time of writing and to our knowledge, structures of only a few macromolecular complexes <80 kDa have been determined using cryo-EM[33-37]. The structure of the KBP-KIF15_MD6S complex shows how KBP binds the KIF15_MD6S via its concave face and undergoes subtle remodelling of its N-terminal domain to accommodate kinesin binding. This further reinforces the idea that the TPR-containing structures are not simply static scaffolds but can flexibly respond to ligand binding[38]. In contrast, the KIF15 motor domain undergoes a radical conformational change in forming a complex with KBP, in which helix α4, the major component of the motor's tubulin-binding subdomain, is displaced from the main MD body by ~15 Å into the KBP concave face. This is consistent with previous observations that this region of the kinesin motor domain being rather malleable and able to move independently of the core structure of kinesin motor domains[39,40]. Our evidence suggests this observation is not due to use of a cysteine-substituted KIF15 motor domain construct because: i) this protein exhibited equivalent MT-stimulated ATPase activity compared to non-substituted KIF15_MD (Figure 2 – figure supplement 2a), ii) it exhibited structurally canonical MT binding and response to nucleotide (Figure 3 – figure supplement 1), and iii) the substituted residues are not well conserved among KBP-binding kinesins (Figure 6a). The large displacement of helix α4 expands the surface area over which the normally compact tubulin-binding subdomain of the kinesin motor domain can interact with KBP, and it is through the

sequence and shape of this interface that the selectivity of KBP for a subset of kinesin motors is presumably defined.

Analysis of the KBP-KIF1A_MD complex (Figure 2–figure supplement 1c) supports the idea of a conserved mode of interaction between a subset of kinesins and the concave face of KBP. Interestingly, KIF1A_MD exhibited flexibility in its interaction with KBP, which was not observed in the KBP-KIF15_MD6S complex. Whether this reflects a physiological reality, or a result of the EM preparation method is uncertain at present, although we think it unlikely to be due to our use of KIF15_MD6S. However, our 2D classifications combined with mutation studies strongly suggest KIF15_MD6S and KIF1A_MD share an overall similar KBP binding mode.

Targeted mutations to the various kinesin-binding KBP elements reduced complex affinity, yet no single mutation completely disrupted the interaction in our pull-down assays (Figure 5- figure supplement 2). In contrast, in the context of active MT-based cargo translocation in the cellular environment, KBP inhibitory activity appeared more sensitive to disruption (Figure 5 d-g). Although most KBP mutations that have been reported in GOSHS result in total loss of protein[11-14], a recent study details missense mutations that only partially reduce protein expression (MacKenzie et al, 2020). Our data illustrate that KBP's activity is additionally sensitive to mutations in key regions that affect its ability to bind kinesins.

Our structure shows that KBP binds exclusively to the tubulin-binding subdomain of KIF15_MD6S, sterically preventing MT attachment. The interaction of kinesin motor domains with the MT surface via its tubulin-binding subdomain stimulates nucleotide exchange and kinesin ATPase activity. In contrast, on interaction with KBP, the displacement of helix α4 from the kinesin nucleotide-

388 binding site, together with the absence of MT-mediated ordering of KL9 and KL11,
389 means that its catalytic site is distorted and the structural changes associated with MT-
390 stimulated ATPase cannot occur. This could be an important facet of the role of KBP
391 in the energy economy of the cell in addition to directly blocking kinesin-MT
392 interactions.

393 The concave face of TPR-containing α-solenoids commonly serve as a
394 recognition platform for specific peptide motifs, including those forming α-helical
395 structures[41]. Specificity and affinity for target motifs are determined in part by the
396 shape of the α-solenoid concave face, which in turn is defined by the fold's
397 supertwist. In addition, particular amino-acid arrangements at the concave face
398 contribute to partner binding affinity and specificity, together with additional
399 interfaces formed at the convex surface or α-solenoid edge[42]. KBP kinesin specificity
400 and affinity is defined by the interaction of its concave face with the large surface area
401 of the kinesin L11-Kα4-KL12-Kα5-KL13 region, in addition to binding the kinesin
402 Kβ5-KL8 region at its α-solenoid edge. Interestingly, distal to the N-terminal MT-
403 binding region of kinesin-1, C-terminally-associated kinesin light chain use their
404 unique TPR-containing α-solenoid concave face to select cargos via recognition of
405 specific peptide motifs[43]. Therefore, peptide selectivity by TPR-containing α-
406 solenoids is a facet of both kinesin MT-binding and cargo-binding regulatory
407 mechanisms. Such protein-protein interactions may be selectively targeted for
408 disruption[44], and the insights arising from our work provide future avenues to disrupt
409 KBP-kinesin interactions and thereby explore KBP interactions and regulatory roles.

410 The effective and selective kinesin inhibitory mechanism of KBP revealed by
411 our work may fulfil specific roles in the kinesin regulatory toolbox employed by cells
412 to spatially and temporarily orchestrate kinesin activity. Future studies will be aimed

at understanding how KBP interacts with kinesins in dimeric and/or autoinhibited forms. For example, while KBP does not interact with some target kinesins in autoinhibited conformations[18], others that retain a structurally available tubulin-binding subdomain, such as autoinhibited kinesin-3 monomers[45], are feasible binding partners. KBP can bind to constitutively active dimeric kinesin constructs that lack autoinhibitory regions[9,18], although the stoichiometry and structural details in this context are unclear. Furthermore, any additional effects of kinesin cargo binding on their susceptibility to KBP inhibition are not well understood. It will also be of key importance to elucidate the mechanisms of KBP activity regulation, for example, by phosphorylation of KBP and/or kinesins[9] and KBP acetylation and targeted degradation by the ubiquitin system[46]. Our structural characterisation of the KBP-kinesin inhibitory interaction provides an important mechanistic platform from which to expand our understanding of KBP's biological roles in neuronal function and cancer.

Methods

Protein expression and purification for cryo-EM

Full length human KBP residues 1-621 in a PSTCm1 expression vector (with kanamycin resistance and a N-terminal thrombin cleavable 6 x His-tag) was expressed in Rosetta2 cells (Novagen) as previously described[9]. Following immobilised metal-affinity chromatography with Ni-NTA resin (Qiagen), the 6 x His-tag was removed via incubation with thrombin protease overnight at 4 °C. The protein was then subjected to reverse IMAC and further purified using size exclusion chromatography (SEC) into a buffer of 20mM TrisHCL (pH7.4), 150mM NaCl, 2.5mM CaCl2, 1mM DTT. Protein was snap-frozen and stored in at -80 °C.

A human KIF15 motor domain and neck linker construct (residues 1-375) in a pET21a vector with a C-terminal 6 x His-tag was generated by chemical synthesis (GenScript, Piscataway, NJ). Six of the eight cysteine residues (C5S, C50S, C162S, C294S, C314S, C346S) were mutated and two cysteines were inserted (S250C, G375C) for orthogonal experiments not described further here. We refer to this construct as KIF15_MD6S. KIF15_MD6S was expressed and purified using methods previously described[47], then buffer exchanged into 25 mM HEPES pH 7.5, 100 mM KCl, 2 mM MgCl2, 1 mM EGTA, 1 mM DTT, 0.1 mM ATP, snap frozen in liquid nitrogen and stored at -80ºC.

A human KIF1A motor domain and neck linker construct (KIF1A_MD residues 1-362) in a pFN18a vector (with a TEV protease-cleavable N-terminal Halo-tag and a C-terminal 6 x His-tag) was expressed in BL21-Gold (DE3) cells, as previously described[28]. Following a first IMAC with Ni-NTA resin, the Halo-tag was removed

via incubation overnight with TEV protease at 4 °C. The protein was then isolated from TEV via a second IMAC with Ni-NTA resin and further purified by SEC into a storage buffer of (20 mM HEPES, pH 7, 150 mM NaCl, 5 mM $MgCl_2$, 0.1 mM ADP and 1 mM TCEP).

KIF15_MD6S or KIF1A_MD complexes with KBP were purified via IMAC using the 6 x His tag on the kinesin constructs. Briefly, His-tagged kinesins were incubated with a 10 times excess of KBP in 20 mM TrisHCL (pH7.5), 150 mM NaCl, 1 mM $MgCl_2$, 10 mM Imidazole, 1 mM DTT, 0.2 mM ADP for 5 minutes at 4 °C. Following IMAC, complexes were eluted from the Ni-NTA resin (Qiagen) by addition of 200 mM imidazole, then dialyzed at 4 °C for 4 hours into 20 mM TrisHCL (pH7.5), 150 mM NaCl, 1 mM $MgCl_2$, 1 mM DTT, 0.2 mM ADP.

Steady-state ATPase assay

ATPase activity of KIF15_MD6S was measured in ATPase buffer (50 mM potassium acetate, 25 mM HEPES, 5 mM magnesium acetate, 1 mM EGTA, pH 7.50) by measuring phosphate production in the presence of a minimum of a 5-fold molar excess of paclitaxel-stabilised MTs, using a commercially-available kit (EnzChek, Molecular Probes) at 20^{o}C.

Sample preparation for cryo-EM

KBP was prepared for cryo-EM using three different approaches. In the first approach, KBP was diluted to 0.15 mg/ml in KBP dilution buffer (20 mM TrisHCL, pH7.5, 150 mM NaCl, 2 mM DTT) and 4 µl were applied to glow-discharged C-

flat™ 2/2 holey carbon EM grids (Protochips, Morrisville, NC). For the second approach, KBP was diluted to 0.3 mg/ml in KBP dilution buffer and 4 µl were applied to glow-discharged 1.2/1.3 AuFoil gold grids (Quantifoil®). For the third approach, glow-discharged C-flat™ 2/2 holey carbon EM grids were coated with graphene-oxide (GO) according to the protocol described by Cheng and colleagues[48] then 4 µl of KBP diluted to 0.02 mg/ml in KBP dilution buffer were added.

Kinesin motor domain-KBP complexes were diluted to 0.03 mg/ml in KBP-kinesin dilution buffer (20 mM TrisHCL (pH7.5), 50 mM NaCl, 1 mM $MgCl_2$, 1 mM DTT, 0.2 mM ADP) and 4 µl were added to the GO-coated gold grids described above. After a 30 second incubation of samples on the EM grid in a Vitrobot Mark IV (FEI Co., Hillsboro, OR) set at 4 °C and 80 % humidity, samples were blotted (6-8 seconds, blot force -10) and vitrified in liquid ethane. All steps were performed at 4 °C.

For preparation of the KIF15_MD6S-MT complex, porcine tubulin (>99% pure, Cytoskeleton Inc.) was polymerised in MES polymerisation buffer (100 mM MES, 1 mM $MgCl_2$, 1 mM EGTA, 1 mM DTT, pH 6.5) with 5 mM GTP at 37 °C then stabilised with 1 mM paclitaxel. ~70 µM KIF15_MD6S was pre-incubated for 5 min with 5 mM of AMPPNP in BRB80 at room temperature, and then mixed with 20 µM stabilised MTs. After a further incubation of 15 min, a 4 µl droplet was applied to a pre-glow discharged holey carbon grid (2/2 C-flat, Protochips Inc.), blotted for 3.5 s and then vitrified in liquid ethane using a Vitrobot Mark IV at ambient temperature and 80% humidity.

Cryo-EM data collection

For dataset of KBP alone or KBP-KIF15_MD6S, low-dose movies were collected automatically using EPU software (Thermo Fisher, MA, USA) on a Titan Krios electron microscope (Thermo Fisher) operating at 300 kV, with a K2 summit direct electron detector (Gatan, CA, USA) and a quantum post-column energy filter (Gatan) operated in zero-loss imaging mode.

Datasets of KBP alone were collected either at eBIC or the ISMB, Birkbeck using a Volta phase plate (VPP), a sampling of ~1.05 Å/pixel and a nominal defocus range of 0.5-0.7 μm. The total dose was 42 e-/Å^2 over 40 frames, with the detector operating in counting mode at a rate of ~5 e-/pixel/second.

Datasets of KBP-kinesin complexes were collected at the ISMB, Birkbeck without a phase plate and a nominal defocus range of 1.5-4 μm. KIF1A_MD-KBP complexes were collected at a sampling of 0.85 Å/pixel, whereas KBP-KIF15_MD6S complexes were collected at a sampling of 1.047 Å/pixel. For KIF1A_MD-KBP complexes, the total dose was 88 e-/Å^2 over 36 frames, with the detector operating in counting mode at a rate of 7.1 e-/pixel/second. For KBP-KIF15_MD6S complexes, the total dose was 80 e-/Å^2 over 64 frames, with the detector operating in counting mode at a rate of 5.7 e-/pixel/second.

The KIF15_MD6S-MT dataset was collected manually on a Tecnai Polara microscope (Thermo Fisher) at the ISMB, Birkbeck, operating at 300 kV, with a K2 summit direct electron detector (Gatan, CA, USA) and a quantum post-column energy filter (Gatan) operated in zero-loss imaging mode. A nominal defocus range of 1.0-3.5 μm and a final pixel size of 1.39 Å was used. The total dose was 32 e-/Å^2 over 50 frames, with the detector operating in counting mode at a rate of 6.2 e-/pixel/second.

Cryo-EM data processing

Low-dose movies were motion-corrected using MotionCor2[49] with a patch size of 5, generating full-dose and dose-weighted sums. CTF determination was performed on full-dose sums with gCTF[50] and then dose-weighted sums were used for all further processing. Data were cleaned at this stage by first excluding all micrographs with gCTF resolutions worse than 4.5 Å, as estimated with a custom cross-correlation coefficient cutoff (Python script kindly shared by Radostin Danev), then manually removing micrographs with poor appearance (ice contamination, protein aggregation or poor GO coverage) in real or reciprocal space. For KBP alone data, micrographs with calculated phase shifts outside the expected phase shift progression at each plate position were also excluded.

Particles were first picked using Eman2's neural network picker[51], with a 180 pixel box size for KBP-alone and KBP-KIF15_MD6S datasets, or a 220 pixel box size for the KBP-KIF1A_MD datasets. Good 2D classes were then used as templates to pick the data with Gautomatch (http://www.mrc-lmb.cam.ac.uk/kzhang/).

For Eman2 neural network picker or Gautomatch-derived particles from each dataset, separate multiple rounds of 2D classification were performed in RELION v3.0[52], cryoSPARC2[53] or cisTEM[54]. This resulted in a total of six sets of good 2D classes showing clear secondary structure for each dataset, two produced by each programme for each picking method. For each dataset, these six good 2D class sets for each dataset were then combined and duplicate particles removed. At this stage, for each sample (KBP-alone, KBP-KIF15_MD6S or KBP-KIF1A_MD) good 2D classes from their constituent datasets were combined.

KBP-KIF15_MD6S or KBP-KIF1A_MD datasets, composed of their respective constituent datasets were easily combined, being from the same microscope and

554 optical set up. However, KBP-alone data were collected on different microscopes and
555 had a range of pixel sizes (<2% difference). KBP-alone data therefore was combined
556 at this stage using the optics grouping protocol in RELION v3.1[52].
557 KBP-alone and KBP-KIF15_MD6S data were taken to 3D processing at this
558 stage, while multiple attempts to process KBP-KIF1A_MD data in 3D gave no
559 reliable results. For KBP-alone and KBP- KIF15_MD6S data, *de novo* initial 3D
560 models were created in cryoSPARC2. For KBP- KIF15_MD6S data, a single round of
561 3D classification was performed in RELION v3.0 and the best class selected and
562 auto-refined. For KBP-alone data, 3D classification in RELION v3.1 or cryoSPARC2
563 did not reveal different 3D structures or improve reconstructions over sorting only in
564 2D; therefore, particles selected with 2D classification were used as direct input for
565 auto-refinement. The final KBP-alone map was sharpened with a B-factor of -200 to
566 the gold-standard FSC 0.143 cutoff (4.6 Å). The KBP- KIF15_MD6S map was
567 sharpened locally with a B-factor of -495, according to local resolutions determined
568 using RELION v3.1's inbuilt local resolution software.
569 The KIF15_MD6S-MT dataset was processed using our MT RELION-based
570 pipeline (MiRP) as described previously, using low-pass filtered KIF5B_MD-
571 decorated MTs as references [55,56]. KIF15_MD6S 13-protofilament-MTs were the
572 most common MT architecture and were selected after supervised 3D classification in
573 MiRP for analysis. The symmetrised asymmetric unit (KIF15_MD6S plus a tubulin
574 dimer) was locally sharpened in UCSF Chimera with a B-factor of -134 according to
575 local resolutions determined using RELION v3.0's inbuilt local resolution software.
576 All displayed 3D molecular representations were made in UCSF Chimera or
577 ChimeraX software[57,58]. Data collection and model refinement statistics can be found
578 in Table 1..

Cryo-EM model building and refinement

Due to low overall homology to available structures in the protein data bank (PDB), structure prediction of KBP produced poor models with little resemblance to the cryo-EM density. KBP was therefore modelled using a combination of secondary structure prediction, TPR prediction, fragment homology information, prior knowledge of right-handed alpha-solenoid proteins and with reference to the cryo-EM density.

TPR motifs were identified in the KBP sequence using the TPRpred server[59] available in the MPI Bioinformatics Toolkit[60]. Secondary structure predictions using Raptor X[61], iTasser[62], JPred[63], Spider2[64], PSSpred[65] and SOPMA[66] were then run on the sequence and consensus between these multiple predictions used to assign likely α-helical content. To identify regions dispensable for the overall fold and likely disordered loop regions, disorder prediction was performed with Raptor X and inter-species low homology regions in KBP (from early Metazoans to humans) were determined via Clustal Omega multiple sequence alignment[67]. Finally, weak homology models for overlapping fragments of the structure were identified using the HHpred[68] server in the MPI Bioinformatics Toolkit.

With the information described above a sequence alignment was built with KBP and the following fragment homology model PDBs; 5OJ8, 4A1S, 3QC1, 4NQ0, 4AIF, and 5MX5. This sequence alignment was used as a basis for multiple rounds of modelling and flexible fitting with Modeller[69] and Flex-EM[70] respectively, using α-helical secondary structure restraints. This modelling process was guided by consistency with the cryo-EM density and secondary structure and TPR predictions described above. Finally, the structure was refined against the cryo-EM density in

real-space with 5 macro-cycles in Phenix[71]. All 19 predicted and modelled helices were accounted for by rod-like cryo-EM density in the reconstruction and at 4.6 Å resolution, density was discernible for bulky side chains in the TPR regions (Figure 1–figure supplement 1a,b), providing a validation of the assigned sequence directionality in the fold.

The KBP KIF15_MD6S model was built as follows: the final KBP model described above and the KIF15_MD x-ray crystallographic model (PDB code:4BN2[25]) were rigid fitted into the KBP-KIF15_MD6S density in Chimera. Density for an extended α6-helix and docked neck-linker in KIF15_MD6S were absent; therefore, Modeller was used to model a short α6-helix and the neck-linker removed. A model for the L11, α4-helix and L12 region in KIF15_MD6S were then created using Coot[72] and Modeller. The model was refined into the cryo-EM density in real-space using Phenix[7] with secondary structure restraints. A first refinement of 15 cycles used rigid bodies describing α-helical hairpins in KBP to get a good rough fit. Following this, the whole complex was further refined without rigid bodies for another 5 macro-cycles.

The KIF15_MD6S-MT model was built as follows: the KIF15_MD, KIF11_MD and KIF5B_MD-tubulin x-ray crystallographic models (PDB codes:4BN2[25,27,73]) were used as homology models in Modeller to build the KIF15 part of the complex. The KIF15_MD6S model and the paclitaxel-MT tubulin dimer model[74] were then rigid fitted into KIF15_MD6S -MT density, combined then refined in real-space with 5 macro-cycles in Phenix with peptide backbone restraints.

Antibodies, reagents and expression constructs for cell biology

The following antibodies were used for immunofluorescence staining: mouse anti-HA (1:500, Roche), and goat-anti-mouse Alexa 488 (1:400, Thermo Fisher Scientific). The following antibodies were used for western blot: mouse anti-HA (1:2,000, BioLegend), rabbit anti-GFP (1:10,000, Abcam), goat anti-mouse IRDye800CW (1:15.000, LI-COR), and goat-anti-rabbit IRDye680LT (1:20,000, LI-COR). A reagent used in this study is rapalog (AP21967, TaKaRa).

The following DNA expression constructs in this study have been described before: GW1-PEX3-mRFP-FKBP1, βactin-Kif1A_MDC-FRB[9] (mouse cDNA), BirA coding vector[75] and pebioGFP[75]. pGW1-HA-KBP contained a linker (GGATCCCCGGAATTCGGCACGAGGGAGGCCGCT) between the HA tag and KBP and was cloned using PCR based strategies with human KBP cDNA (KIAA1279, IMAGE clone 4550085) as template and ligation into the pGW1-HA backbone. A similar strategy was used to generate the mutated KBP constructs, listed in Table 2. βactin-KIF15_MDC-FRB was cloned using a PCR based Gibson Assembly strategy with mouse KIF15 cDNA as template into the βactin-KIF1A_MDC-FRB backbone. PebioGFP-KIF1A_MDC and pebioGFP-KIF15_MDC were cloned into the pebioGFP backbone using PCR based strategies with MDC-FRB constructs as templates.

Cell culture, transfection and immunofluorescence staining

COS-7 cells were purchased from ATCC and routinely checked for mycoplasma contamination using LT07-518 Mycoalert assay (Lonza). Cells were cultured in 50/50 DMEM (Lonza)/Ham's F10 (Lonza) medium supplemented with 10% FCS (Sigma) and 1% penicillin/streptomycin (Sigma). One day before transfection cells were

diluted and plated on 18-mm glass coverslips. COS-7 cells were transfected using FuGENE6 (Roche) following the manufacturer's protocol. Next day, rapalog (final concentration 1 µM) was added and cells were incubated for 3 hours. Cells were then fixed with 4% formaldehyde/4% sucrose in phosphate-buffered saline (PBS) for 10 minutes at room temperature, washed three times PBS-CM (PBS supplemented with 1 mM $MgCl_2$ and 0.1 mM $CaCl_2$), permeabilized in 0.2% TritonX-100 for 15 minutes and washed one time with PBS-CM. Cells were first incubated with 0.2% gelatin for 30 minutes at 37 ℃, and then with primary antibodies, diluted in 0.2% gelatin, for 30 minutes at 37 ℃. After washing three times with PBS-CM, cells were incubated for 30 minutes at 37 ℃ with secondary antibody diluted in 0.2% gelatin, washed three times in PBS-CM, and finally mounted using Fluoromount (Invitrogen).

Cell biology image analysis and quantification

Fixed cells were imaged on a Carl Zeiss LSM 700 confocal laser scanning microscope running ZEN2011 software, using a Plan-Apochromat 40x/1.30 oil DIC objective and image settings were maintained the same for all images within one experiment. Images were acquired of cells that express similar levels of HA-KBP constructs based on immunostaining (Figure 5 – figure supplement 1). Cells were selected on a first-come-first served basis. Images were processed and analysed using Fiji software[76]. To calculate the percentage of cells in which translocation of peroxisomes was observed, imaged cells were classified as either translocating, when peroxisomes re-localized into the cell periphery, or not translocating, when peroxisomes remained in the cell centre. For quantification of PEX translocation, an ROI of the cell area was drawn and from this a second ROI at 5 (KIF1A_MDC) or 7.5 (KIF15_MDC) µm from the

outer cell area was created. Images were thresholded at 7500 (KIF15_MDC) or 10000 (KIF1A_MDC). Different peripheral areas and threshold values were defined for the two kinesins, due to observed differences in translocation properties between the kinesins (compare Figure 5 – figure supplement 3a-c). For the two selected ROIs, the area with fluorescent intensity above threshold was determined in the RFP channel. From these values the percentage of cell area above threshold in the cell periphery from the total area above threshold was calculated.

Pull-down experiments and western blotting

HEK293T cells were purchased from ATCC and routinely checked for mycoplasma contamination using LT07-518 Mycoalert assay (Lonza). Cells were cultured in 50/50 DMEM (Lonza)/Ham's F10 (Lonza) medium supplemented with 10% FCS (Sigma) and 1% penicillin/streptomycin (Sigma). One day before transfection cells were diluted and plated into 6-well plates. Cells were co-transfected with pCl-Neo-BirA, HA-tagged constructs and bioGFP-tagged constructs using MaxPEI (Polysciences) in a ratio of 3/1 PEI/DNA, according to the manufacturer's protocol. After 24-hours of expression, cells were washed in ice-cold PBS and lysed in lysis buffer (100 mM TrisHCl pH 7.5, 150 mM NaCl, 1% Triton X-100, protease inhibitors (Roche)) for 30 minutes on ice. Lysates were cleared by 30-minute centrifugation at 13.2 krpm at 4°C and supernatants were incubated with blocked (incubation for 30 minutes at RT in 50 mM Tris–HCl pH 7.5, 150 mM KCl, 0.2 µg/µl chicken egg albumin) Streptavidin Dynabeads M-280 (Invitrogen) for 1.5 hours at 4°C. Beads were then washed five times with washing buffer (100 mM Tris–HCl pH 7.5, 250 mM NaCl, 0.5% Triton X-100) and proteins were eluded from the beads by boiling for 10 minutes at 95°C in 2x

DTT+sample buffer (20% glycerol, 4% SDS, 200 mM DTT, 100 mM Tris–HCl pH 6.8, bromophenol blue).

Protein samples were run on 10% SDS-PAGE gels and transferred to nitrocellulose membranes (Bio-Rad) by semi-dry blotting at 16V for 1 hour. Membranes were blocked by incubation in 3% bovine serum albumin (BSA) in PBST (PBS supplemented with 0.02% Tween20) for 1 hour at room temperature. This was followed by overnight incubation with primary antibodies in 3% BSA-PBST. Membranes were washed three times with PBST, incubated with secondary antibody in 3% BSA-PBST for 1 hour at room temperature, and washed three times with PBST. Membranes were scanned using an Odyssey Infrared Imaging system (LI-COR Biosciences) and blots were acquired at 680 nm and 800 nm.

Acknowledgements

J.A. was supported by a grant from the Medical Research Council (MRC), U.K. (MR/R000352/1) to C.A.M, J.L. and A.P were supported by a grant from Worldwide Cancer Research, U.K. (16-0037) awarded to J.L and C.A.M. We thank Dr Alexander Cook for technical and processing assistance at the ISMB and Dr Radostin Danev at the Graduate School of Medicine, The University of Tokyo for custom processing scripts. Cryo-EM data collected at the Institute of Structural and Molecular Biology (ISMB), Birkbeck was on equipment funded by the Wellcome Trust, U.K. (202679/Z/16/Z, 206166/Z/17/Z and 079605/Z/06/Z) and the Biotechnology and Biological Sciences Research Council (BBSRC) UK (BB/L014211/1). We thank Dr Natasha Lukoyanova for support during data collection at the ISMB. For the remaining EM data collection, we acknowledge Diamond for access and support to

the Electron Bioimaging Centre (eBIC) at Diamond, Harwell, UK, funded by the MRC, BBSRC and Wellcome Trust, U.K. S.S.R. was supported by a grant from the National Institute of General Medical Sciences (R01GM130556). N.O and M.O.S were supported by a grant awarded to M.O.S from the Swiss National Science Foundation (31003A_166608). J.J.A. was supported by the Netherlands Organization for Scientific Research (NWO-ALW-VICI, CCH), and the European Research Council (ERC) (ERC-consolidator, CCH).

The authors have no competing financial interests

References

1. Vale, R.D. The molecular motor toolbox for intracellular transport. *Cell* **112**, 467-80 (2003).
2. Hirokawa, N., Noda, Y., Tanaka, Y. & Niwa, S. Kinesin superfamily motor proteins and intracellular transport. *Nat Rev Mol Cell Biol* **10**, 682-96 (2009).
3. Klinman, E. & Holzbaur, E.L.F. Walking Forward with Kinesin. *Trends Neurosci* **41**, 555-556 (2018).
4. Lawrence, C.J. et al. A standardized kinesin nomenclature. *J Cell Biol* **167**, 19-22 (2004).
5. Miki, H., Setou, M., Kaneshiro, K. & Hirokawa, N. All kinesin superfamily protein, KIF, genes in mouse and human. *Proc Natl Acad Sci U S A* **98**, 7004-11 (2001).
6. Hirokawa, N., Niwa, S. & Tanaka, Y. Molecular motors in neurons: transport mechanisms and roles in brain function, development, and disease. *Neuron* **68**, 610-38 (2010).
7. Mandelkow, E. & Mandelkow, E.M. Kinesin motors and disease. *Trends Cell Biol* **12**, 585-91 (2002).
8. Wozniak, M.J., Melzer, M., Dorner, C., Haring, H.U. & Lammers, R. The novel protein KBP regulates mitochondria localization by interaction with a kinesin-like protein. *BMC Cell Biol* **6**, 35 (2005).
9. Kevenaar, J.T. et al. Kinesin-Binding Protein Controls Microtubule Dynamics and Cargo Trafficking by Regulating Kinesin Motor Activity. *Curr Biol* **26**, 849-61 (2016).
10. Alves, M.M. et al. KBP interacts with SCG10, linking Goldberg-Shprintzen syndrome to microtubule dynamics and neuronal differentiation. *Hum Mol Genet* **19**, 3642-51 (2010).
11. Brooks, A.S. et al. Homozygous nonsense mutations in KIAA1279 are associated with malformations of the central and enteric nervous systems. *Am J Hum Genet* **77**, 120-6 (2005).
12. Dafsari, H.S. et al. Goldberg-Shprintzen megacolon syndrome with associated sensory motor axonal neuropathy. *Am J Med Genet A* **167**, 1300-4 (2015).
13. Valence, S. et al. Homozygous truncating mutation of the KBP gene, encoding a KIF1B-binding protein, in a familial case of fetal polymicrogyria. *Neurogenetics* **14**, 215-24 (2013).
14. Salehpour, S., Hashemi-Gorji, F., Soltani, Z., Ghafouri-Fard, S. & Miryounesi, M. Association of a Novel Nonsense Mutation in KIAA1279 with Goldberg-Shprintzen Syndrome. *Iran J Child Neurol* **11**, 70-74 (2017).
15. Tanaka, H., Ito, J., Cho, K. & Mikawa, M. Hirschsprung disease, unusual face, mental retardation, epilepsy, and congenital heart disease: Goldberg-Shprintzen syndrome. *Pediatr Neurol* **9**, 479-81 (1993).
16. Suo, C. et al. Accumulation of potential driver genes with genomic alterations predicts survival of high-risk neuroblastoma patients. *Biol Direct* **13**, 14 (2018).

17. Brouwers, N., Mallol Martinez, N. & Vernos, I. Role of Kif15 and its novel mitotic partner KBP in K-fiber dynamics and chromosome alignment. *PLoS One* **12**, e0174819 (2017).
18. Malaby, H.L.H., Dumas, M.E., Ohi, R. & Stumpff, J. Kinesin-binding protein ensures accurate chromosome segregation by buffering KIF18A and KIF15. *J Cell Biol* **218**, 1218-1234 (2019).
19. Lehti, M.S., Kotaja, N. & Sironen, A. KIF1-binding protein interacts with KIF3A in haploid male germ cells. *Reproduction* **150**, 209-16 (2015).
20. Lyons, D.A., Naylor, S.G., Mercurio, S., Dominguez, C. & Talbot, W.S. KBP is essential for axonal structure, outgrowth and maintenance in zebrafish, providing insight into the cellular basis of Goldberg-Shprintzen syndrome. *Development* **135**, 599-608 (2008).
21. Drevillon, L. et al. KBP-cytoskeleton interactions underlie developmental anomalies in Goldberg-Shprintzen syndrome. *Hum Mol Genet* **22**, 2387-99 (2013).
22. Drerup, C.M., Lusk, S. & Nechiporuk, A. Kif1B Interacts with KBP to Promote Axon Elongation by Localizing a Microtubule Regulator to Growth Cones. *J Neurosci* **36**, 7014-26 (2016).
23. Chang, H.Y., Cheng, H.Y., Tsao, A.N., Liu, C. & Tsai, J.W. Multiple Functions of KBP in Neural Development Underlie Brain Anomalies in Goldberg-Shprintzen Syndrome. *Front Mol Neurosci* **12**, 265 (2019).
24. Hirst, C.S. et al. Kif1bp loss in mice leads to defects in the peripheral and central nervous system and perinatal death. *Sci Rep* **7**, 16676 (2017).
25. Klejnot, M. et al. The crystal structure and biochemical characterization of Kif15: a bifunctional molecular motor involved in bipolar spindle formation and neuronal development. *Acta Crystallogr D Biol Crystallogr* **70**, 123-33 (2014).
26. Shang, Z. et al. High-resolution structures of kinesin on microtubules provide a basis for nucleotide-gated force-generation. *Elife* **3**, e04686 (2014).
27. Gigant, B. et al. Structure of a kinesin-tubulin complex and implications for kinesin motility. *Nat Struct Mol Biol* **20**, 1001-7 (2013).
28. Atherton, J. et al. Conserved mechanisms of microtubule-stimulated ADP release, ATP binding, and force generation in transport kinesins. *Elife* **3**, e03680 (2014).
29. Atherton, J. et al. The divergent mitotic kinesin MKLP2 exhibits atypical structure and mechanochemistry. *Elife* **6**(2017).
30. Culurgioni, S., Alfieri, A., Pendolino, V., Laddomada, F. & Mapelli, M. Inscuteable and NuMA proteins bind competitively to Leu-Gly-Asn repeat-enriched protein (LGN) during asymmetric cell divisions. *Proc Natl Acad Sci U S A* **108**, 20998-1003 (2011).
31. Wang, J., Dye, B.T., Rajashankar, K.R., Kurinov, I. & Schulman, B.A. Insights into anaphase promoting complex TPR subdomain assembly from a CDC26-APC6 structure. *Nat Struct Mol Biol* **16**, 987-9 (2009).
32. Quinaud, M. et al. Structure of the heterotrimeric complex that regulates type III secretion needle formation. *Proc Natl Acad Sci U S A* **104**, 7803-8 (2007).
33. Merk, A. et al. Breaking Cryo-EM Resolution Barriers to Facilitate Drug Discovery. *Cell* **165**, 1698-1707 (2016).

34. Zhang, K. et al. Structure of the 30 kDa HIV-1 RNA Dimerization Signal by a Hybrid Cryo-EM, NMR, and Molecular Dynamics Approach. *Structure* **26**, 490-498 e3 (2018).
35. Khoshouei, M., Radjainia, M., Baumeister, W. & Danev, R. Cryo-EM structure of haemoglobin at 3.2 A determined with the Volta phase plate. *Nat Commun* **8**, 16099 (2017).
36. Herzik, M.A., Jr., Wu, M. & Lander, G.C. High-resolution structure determination of sub-100 kDa complexes using conventional cryo-EM. *Nat Commun* **10**, 1032 (2019).
37. Fan, X. et al. Single particle cryo-EM reconstruction of 52 kDa streptavidin at 3.2 Angstrom resolution. *Nat Commun* **10**, 2386 (2019).
38. Pernigo, S. et al. Structural basis for isoform-specific kinesin-1 recognition of Y-acidic cargo adaptors. *Elife* **7**(2018).
39. Wang, D. et al. Motility and microtubule depolymerization mechanisms of the Kinesin-8 motor, KIF19A. *Elife* **5**(2016).
40. Scarabelli, G. & Grant, B.J. Mapping the structural and dynamical features of kinesin motor domains. *PLoS Comput Biol* **9**, e1003329 (2013).
41. Perez-Riba, A. & Itzhaki, L.S. The tetratricopeptide-repeat motif is a versatile platform that enables diverse modes of molecular recognition. *Curr Opin Struct Biol* **54**, 43-49 (2019).
42. Zeytuni, N. & Zarivach, R. Structural and functional discussion of the tetra-trico-peptide repeat, a protein interaction module. *Structure* **20**, 397-405 (2012).
43. Cross, J.A. & Dodding, M.P. Motor-cargo adaptors at the organelle-cytoskeleton interface. *Curr Opin Cell Biol* **59**, 16-23 (2019).
44. Randall, T.S. et al. A small-molecule activator of kinesin-1 drives remodeling of the microtubule network. *Proc Natl Acad Sci U S A* **114**, 13738-13743 (2017).
45. Ren, J. et al. Coiled-coil 1-mediated fastening of the neck and motor domains for kinesin-3 autoinhibition. *Proc Natl Acad Sci U S A* **115**, E11933-E11942 (2018).
46. Donato, V. et al. The TDH-GCN5L1-Fbxo15-KBP axis limits mitochondrial biogenesis in mouse embryonic stem cells. *Nat Cell Biol* **19**, 341-351 (2017).
47. Rosenfeld, S.S., Xing, J., Jefferson, G.M. & King, P.H. Docking and rolling, a model of how the mitotic motor Eg5 works. *J Biol Chem* **280**, 35684-95 (2005).
48. Cheng, K., Wilkinson, M., Chaban, Y. & Wigley, D.B. A conformational switch in response to Chi converts RecBCD from phage destruction to DNA repair. *Nat Struct Mol Biol* **27**, 71-77 (2020).
49. Zheng, S.Q. et al. MotionCor2: anisotropic correction of beam-induced motion for improved cryo-electron microscopy. *Nat Methods* **14**, 331-332 (2017).
50. Zhang, K. Gctf: Real-time CTF determination and correction. *J Struct Biol* **193**, 1-12 (2016).
51. Bell, J.M., Chen, M., Durmaz, T., Fluty, A.C. & Ludtke, S.J. New software tools in EMAN2 inspired by EMDatabank map challenge. *J Struct Biol* **204**, 283-290 (2018).

888 52. Zivanov, J. et al. New tools for automated high-resolution cryo-EM
889 structure determination in RELION-3. *Elife* **7**(2018).
890 53. Punjani, A., Rubinstein, J.L., Fleet, D.J. & Brubaker, M.A. cryoSPARC:
891 algorithms for rapid unsupervised cryo-EM structure determination. *Nat*
892 *Methods* **14**, 290-296 (2017).
893 54. Grant, T., Rohou, A. & Grigorieff, N. cisTEM, user-friendly software for
894 single-particle image processing. *Elife* **7**(2018).
895 55. Atherton, J. et al. Structural determinants of microtubule minus end
896 preference in CAMSAP CKK domains. *Nat Commun* **10**, 5236 (2019).
897 56. Cook, A.D., Manka, S.W., Wang, S., Moores, C.A. & Atherton, J. A
898 microtubule RELION-based pipeline for cryo-EM image processing. *J*
899 *Struct Biol* **209**, 107402 (2020).
900 57. Pettersen, E.F. et al. UCSF Chimera--a visualization system for exploratory
901 research and analysis. *J Comput Chem* **25**, 1605-12 (2004).
902 58. Goddard, T.D. et al. UCSF ChimeraX: Meeting modern challenges in
903 visualization and analysis. *Protein Sci* **27**, 14-25 (2018).
904 59. Karpenahalli, M.R., Lupas, A.N. & Soding, J. TPRpred: a tool for prediction
905 of TPR-, PPR- and SEL1-like repeats from protein sequences. *BMC*
906 *Bioinformatics* **8**, 2 (2007).
907 60. Zimmermann, L. et al. A Completely Reimplemented MPI Bioinformatics
908 Toolkit with a New HHpred Server at its Core. *J Mol Biol* **430**, 2237-2243
909 (2018).
910 61. Wang, S., Li, W., Liu, S. & Xu, J. RaptorX-Property: a web server for protein
911 structure property prediction. *Nucleic Acids Res* **44**, W430-5 (2016).
912 62. Roy, A., Kucukural, A. & Zhang, Y. I-TASSER: a unified platform for
913 automated protein structure and function prediction. *Nat Protoc* **5**, 725-
914 38 (2010).
915 63. Drozdetskiy, A., Cole, C., Procter, J. & Barton, G.J. JPred4: a protein
916 secondary structure prediction server. *Nucleic Acids Res* **43**, W389-94
917 (2015).
918 64. Yang, Y. et al. SPIDER2: A Package to Predict Secondary Structure,
919 Accessible Surface Area, and Main-Chain Torsional Angles by Deep Neural
920 Networks. *Methods Mol Biol* **1484**, 55-63 (2017).
921 65. Yan, R., Xu, D., Yang, J., Walker, S. & Zhang, Y. A comparative assessment
922 and analysis of 20 representative sequence alignment methods for
923 protein structure prediction. *Sci Rep* **3**, 2619 (2013).
924 66. Geourjon, C. & Deleage, G. SOPMA: significant improvements in protein
925 secondary structure prediction by consensus prediction from multiple
926 alignments. *Comput Appl Biosci* **11**, 681-4 (1995).
927 67. Sievers, F. et al. Fast, scalable generation of high-quality protein multiple
928 sequence alignments using Clustal Omega. *Mol Syst Biol* **7**, 539 (2011).
929 68. Hildebrand, A., Remmert, M., Biegert, A. & Soding, J. Fast and accurate
930 automatic structure prediction with HHpred. *Proteins* **77 Suppl 9**, 128-32
931 (2009).
932 69. Sali, A. & Blundell, T.L. Comparative protein modelling by satisfaction of
933 spatial restraints. *J Mol Biol* **234**, 779-815 (1993).
934 70. Topf, M. et al. Protein structure fitting and refinement guided by cryo-EM
935 density. *Structure* **16**, 295-307 (2008).

71. Afonine, P.V. et al. Real-space refinement in PHENIX for cryo-EM and crystallography. *Acta Crystallogr D Struct Biol* **74**, 531-544 (2018).
72. Emsley, P. & Cowtan, K. Coot: model-building tools for molecular graphics. *Acta Crystallogr D Biol Crystallogr* **60**, 2126-32 (2004).
73. Parke, C.L., Wojcik, E.J., Kim, S. & Worthylake, D.K. ATP hydrolysis in Eg5 kinesin involves a catalytic two-water mechanism. *J Biol Chem* **285**, 5859-67 (2010).
74. Kellogg, E.H. et al. Insights into the Distinct Mechanisms of Action of Taxane and Non-Taxane Microtubule Stabilizers from Cryo-EM Structures. *J Mol Biol* **429**, 633-646 (2017).
75. van der Vaart, B. et al. CFEOM1-associated kinesin KIF21A is a cortical microtubule growth inhibitor. *Dev Cell* **27**, 145-160 (2013).
76. Schindelin, J. et al. Fiji: an open-source platform for biological-image analysis. *Nat Methods* **9**, 676-82 (2012).
77. Pena, A., Sweeney, A., Cook, A.D., Topf, M. & Moores, C.A. Structure of Microtubule-Trapped Human Kinesin-5 and Its Mechanism of Inhibition Revealed Using Cryoelectron Microscopy. *Structure* (2020).
78. Chen, S. et al. High-resolution noise substitution to measure overfitting and validate resolution in 3D structure determination by single particle electron cryomicroscopy. *Ultramicroscopy* **135**, 24-35 (2013).
79. Chen, V.B. et al. MolProbity: all-atom structure validation for macromolecular crystallography. *Acta Crystallogr D Biol Crystallogr* **66**, 12-21 (2010).

Figures

Figure 1. KBP is a TPR-containing right-handed α-solenoid.

(a) Model of KBP (ribbon representation) displayed in experimental cryo-EM density. The N-terminal (olive) and C-terminal (gold) subdomains are separated by a linker region (black). Semi-transparent density is coloured regionally as per the fitted model. The N- and C-termini are shown, with a dotted line representing the disordered C-terminus (not modelled). The linker loop region was not modelled but its density is shown in semi-transparent black. (b) The same as panel a, but rotated 180° around the axis indicated. (c) The same view as in panel a, but with the density removed and α-helices displayed as pipes with their directionality indicated by arrows. The 9 antiparallel α-helical pairs (αHP1 to αHP9) are each coloured separately and labelled, as is the linker α-helix (LαH) and linker loop (LL, dotted line). (d) Ribbon representation of KBP showing the 4 tetratrico peptide repeat (TPR) motifs and the LαH coloured according to the labels. View related to panel c, by a 90° rotation around the indicated axis. (e) Schematic of the KBP showing the position of the TPR motifs between residue 95 and 283 of the N-terminal subdomain and position of the linker region (LαH and LL) between residues 305 and 392.

Figure 2. KBP conformationally adapts to bind KIF15's motor domain via both subdomains

(a) Model of the KBP-KIF15_MD6S complex (ribbon representation) displayed in experimental cryo-EM density. The N-terminal (olive) and C-terminal (gold) subdomains and the linker helix (black) are shown in KBP, while kinesin is coloured in magenta. Semi-transparent density is coloured regionally as per the fitted model

and additional density for the linker loop is shown in semi-transparent black. (b) The same as panel a, but rotated 180° around the axis indicated. (c) The KBP-alone model (light grey ribbons) was superimposed on the KBP-KIF15_MD6S model (opaque ribbons) using Chimera's matchmaker[57]. Colouring and view as in panel b. (d) RMSD in Å for KBP comparing KBP-KIF15_MD6S and superimposed KBP-alone models as in panel c, shown on KBP from the KBP- KIF15_MD6S model. Parts of the KBP model coloured black are disordered/missing in the KBP alone model. The KIF15_MD6S is shown in transparent magenta.

Figure 3. The KIF15 motor domain binds KBP via rearrangement of its tubulin-binding subdomain.

(a) The crystallographic model of the KIF15_MD alone (PDB: 4BN2[25]) was superimposed on the KIF15 region of the KBP-KIF15_MD6S complex, with the KIF15 part of the KBP- KIF15_MD6S complex model hidden. The KIF15_MD6S Switch 1/2 subdomain (Switch 1/2 subdomain) is coloured sienna, the P-loop subdomain (Kin-PLsd) is coloured light pink. The TBsd of the KIF15_MD crystallographic model is shown as pale magenta to illustrate poor fit into density. The KBP subdomains are coloured as labelled. Black arrows indicate unaccounted-for cryo-EM density. Individual secondary structure elements in the tubulin-binding subdomain are labelled. The cryo-EM density for the KBP-KIF15_MD6S complex is shown in mesh and is coloured by proximity (≤ 3.5 Å) to the fitted model. (b) Same as in panel a, but the whole fitted KBP-KIF15_MD6S complex model is shown. The KIF15_MD6S tubulin-binding subdomain (TBsd) is now coloured magenta to indicate good fit into density. (c) Zoomed view of just the TBsd (corresponding to the boxed region in Figure 3–figure supplement 2d), showing just the KIF15_MD-alone

crystallographic model. (d) The TBsd in the KIF15_MD6S-MT model, same view as in panel c. The MT is shown in light grey surface representation. (e) The TBsd in the KBP-KIF15_MD6S model, same view as in panel c. KBP is shown in light grey surface representation and the ~15 Å displacement of helix α4 is indicated by the dashed grey arrow.

Figure 4. KBP binds kinesin MDs via conserved motifs in the α-solenoid edge loops and α-helices at the concave face.

(a) Pseudo-atomic model of the KBP-KIF15_MD6S complex (ribbon representation) displayed in cryo-EM density, using the same viewpoint as Figure 2a, but with the KIF15_MD6S now coloured by subdomain as in Figure 3. The KIF15_MD6S Switch 1/2 subdomain (Kin S1/2 sd) is coloured sienna, the P-loop subdomain (Kin-PLsd) is coloured light pink. The KIF15_MD6S tubulin-binding subdomain (TBsd) is coloured magenta. The KBP subdomains are coloured as labelled. The nine helix pairs of KBP are labelled. Semi-transparent density is coloured regionally as per the fitted model and additional density for the linker loop is shown in semi-transparent black. (b) The same as panel a, but rotated 45° and 15° respectively around the axes indicated. (c) Zoomed view of the region indicated in panel a, with density removed and selected KIF15_MD6S and KBP secondary structure elements labelled. (d) Zoomed view of the region indicated in panel b, with density removed and selected KIF15_MD6S and KBP secondary structure elements labelled.

Figure 5. Disruption of cryo-EM defined KBP-kinesin interface perturbs KBP inhibition of KIF15 and KIF1A-mediated cargo translocation in cells.

(a) Schematic depiction of the inducible peroxisome motility assay, with the kinesin motor domain fused to an FRB domain and PEX fused to an FKBP domain. Addition of rapalog (Rap) links FRB and FKBP and induces peroxisome translocation by kinesin dimers. Expression of KBP inhibits kinesin movement, such that addition of rapalog cannot induce peroxisome translocation. (b) Schematic representation of the inducible peroxisome motility assay in cells. Without rapalog or KBP, peroxisomes localize in the cell center, whereas kinesin moves towards the cell periphery. Rapalog induces peroxisome translocation into the cell periphery, which is inhibited in presence of KBP. (c) Representative images of peroxisomes in COS-7 cells expressing KIF15_MDC-FRB, PEX-mRFP-FKBP and HA (left panels) or HA-KBP (right panels) without and with addition of rapalog . Scale bar, 10 µm. (d, e) Quantification of the percentage of cells in which peroxisome translocation is observed after rapalog treatment in cells expressing KIF15_MDC-FRB (d) or KIF1A_MDC-FRB (e), PEX-mRFP-FKBP, and HA-KBP constructs including the indicated mutants. Data are displayed as mean ± s.e.m. (n=28-35 cells from two independent experiments). (f, g) Quantification of the area above threshold intensity in the outer 5 µm (KIF1A_MDC) or 7.5 µm (KIF15_MDC) of the cell from the total area above threshold intensity in cells expressing KIF15_MDC-FRB (f) or KIF1A_MDC-FRB (g), PEX-mRFP-FKBP, and HA-KBP constructs including the indicated mutants without and with rapalog treatment. Data are displayed as mean ± s.e.m. (n=28-35 cells from two independent experiments).

Figure 6. Conserved motifs in KBP-binding kinesin MDs.

(a) Sequence alignment of the tubulin-binding subdomain from kinesin motor domains, made using Clustal Omega multiple sequence alignment[67]. Residues are

coloured according to standard Clustal X colouring (dependent on residue type and conservation, see http://bioinfolab.unl.edu/emlab/documents/clustalx_doc/clustalx.html#C). Kinesin MD constructs experimentally assessed for KBP interactivity are taken from[9]; strongest interactors are in rows highlighted in darker shades of green, weaker interactors in lighter shades of green and non-interactors in red. Secondary structure element, conservation and charge variation columns, as well as a 'binding consensus' column indicating residues/loop length conserved at the interface (according to the KBP-KIF15_MD6S complex) in KBP-binding but not non-binding kinesins are shown above the alignment. Non-conservation relative to this consensus is shown in boxed sequence; red boxes, non-conservative substitutions, orange boxes, conservative substitutions (general charge/polarity/hydrophobicity retention), cyan boxes, extended loop region, dark blue boxes, truncated loop region. (b) Top panel; view of the Kβ4-KL8 region of the tubulin-binding subdomain in the KBP-KIF15_MD6S model, coloured as in Figure 4. Bottom panel; as in upper panel, but with the KIF11_MD cryo-EM model (PDB: 6TA4[77]) superimposed onto the now hidden KBP-KIF15_MD6S. Note steric clash introduced by KIF11_MD's extended KL8. c) Schematic model of KBP's hypothesised selective kinesin inhibition mechanism. KBP (olive) binds the compatible TBsd of recognised kinesins (magenta) but is incompatible with the TBsd of non-binding kinesins (salmon). For its target kinesins, KBP therefore sterically blocks the TBsd interaction with MTs (grey), preventing activation of kinesin ATPase and motility.

Figure 1–figure supplement 1. KBP reconstruction, structure and loop lengths.

(a) Gold-standard FSC curves between independent masked, unmasked, phase-randomised and corrected half-maps[78] of KBP as calculated by RELION v3.1[52] (4.6 Å resolution at the 'gold-standard' 0.143 FSC cutoff). (b) Density and fitted model for TPR3 of KBP, showing exemplar bulky side chain density that guided modelling. (c) Same view as Figure 1c (upper panel), or rotated 90° around the indicated axis (lower panel), showing only α-helices (semi-transparent white tubes) with their terminal residues coloured, illustrating the edges and faces (concave and convex) of the α-solenoid respectively. (d) Same view as panel c, but now with loops shown and coloured (semi-transparent tube helices have their directionality represented by arrows). Each loop or terminus label has a superscript number indicating their length. (e) Same as panel d, rotated 180° around the indicated axis.

Figure 1–figure supplement 2. KBP loops, sequence, inter-species conservation and experimental mutations.

The human KBP sequence (numbering above), with residues coloured by intra-species sequence identity as indicated in the key. The following species were included in the Clustal Omega multiple sequence alignment[67]; *Homo sapiens, Mus musculus, Gallus gallus, Xenopus tropicalis, Alligator mississippiensis, Danio rerio, Drosophila melanogaster, Amphimedon queenslandica, Stylophora pistillata, Trichoplax adhaerens, Spizellomyces punctatus* and *Salpingoeca rosetta.* Above the sequence, secondary structure elements are indicated, coloured to delineate the nine α-helical pairs and connecting loops. Mutation sites are indicated within each boxed sequence region, labelled to coordinate with Figure 5. Within these boxes, the mutated sequence is shown below the original wild-type sequence.

Figure 1–figure supplement 3. Approximate path of the KBP linker loop.

View of KBP's linker loop, using the same KBP model subdomain colouring and representation as in Fig. 1a-b. Only density for the linker loop is shown and a rough path for the linker loop is indicated with a solid black line. KBP α-helices contacting the linker loop region are labelled.

Figure 2–figure supplement 1. KBP-KIF15_MD6S reconstruction resolution estimation and 2D class analysis of KBP-KIF1A_MD and KBP-KIF15_MD complexes.

(a) KIF15_MD6S MT-activated steady-state ATPase velocity plotted as a function of [MT]. Data were fit to a Michaelis Menten kinetic (pink curve) yielding values for kcat = 2.9 ± 0.5 sec-1 and K0.5,MT = 4.8 ± 1.4 μM; R^2 = 0.97, which are very similar to previously published values for KIF15_MD of kcat = 2.1 sec-1 and K0.5,MT = 3.1 μM[25]. (b) Gold-standard FSC curves between independent masked, unmasked, phase-randomised and corrected half-maps[78] of the KBP-KIF15_MD6S complex as calculated by RELION v3.0[52]. The resolution at the 'gold-standard' 0.143 FSC cutoff is 6.9 Å. (c) Local resolution as calculated by RELION v3.0, shown on the same view as in Figure 2a with coloured density corresponding to the local resolutions indicated in the key. (d) Selected RELION v3.0[52] 2D classes of KBP-KIF15_MD6S (left) and KIF1A_MD-KBP (4 to the right). Densities for the kinesin motor domain and KBP are pseudo-coloured pale magenta and pale orange respectively. Classes have been in-plane rotated such that KBP is seen from roughly the same orientation. Note poor resolution and a variable relative position in the KIF1A_MD. (d) A representative subset of KBP-KIF15_MD6S complex 2D classes, showing multiple orientations.

Figure 3–figure supplement 1. KIF15_MD6S adopts a canonical MT-bound kinesin conformation. (a) Gold-standard FSC curves between independent masked, unmasked, phase-randomised and corrected half-maps[78] of the KIF15_MD6S-MT complex as calculated by RELION v3.0[52]. The resolution at the 'gold-standard' 0.143 FSC cutoff is 4.5 Å. (b) Local resolution as calculated by RELION v3.0, with coloured density corresponding to the local resolutions indicated in the key. (c) The KIF15_MD6S-MT asymmetric unit model in corresponding density. The KIF15_MD6S is coloured by subdomain, bound Mg_{2+}-AMPPNP coloured lilac and α and β-tubulin are coloured light and dark grey respectively, along with their corresponding cryo-EM densities. The same view as in panel b. (d) A view of the KIF15_MD6S-MT asymmetric unit showing a docked conformation of the neck-linker (KNL). Model and density colouring as in panel c. (e) The tubulin binding subdomain of KIF15_MD alone from the crystal structure (PDB code:4BN2[25]). (f) KIF15_MD6S complexed with MTs with only the tubulin-binding subdomain and α and β-tubulin shown, along with the tubulin binding subdomain cryo-EM density (semi-transparent). Kα4 of KIF15_MD6S is extended relative to the crystal structure and KL12 adopts a new conformation on α-tubulin, as indicated by the green dashed lines. Panels d and e show the KIF15_MD6S tubulin-binding subdomain from the same viewpoint.

Figure 3–figure supplement 2. Movement of Kα4 of the Kin TBsd upon KBP binding.

(a) The KIF15_MD alone crystal structure (PDB code:4BN2[25]) is shown coloured by kinesin subdomain (as in Figure 3), fitted into the KBP-KIF15_MD6S complex cryo-EM map, with only density shown for the Mg_{2+}-ADP as mesh. Density for Mg_{2+}-ADP

is found in the expected position between nucleotide binding elements KL9, KL11, Kα2a and the P-loop. (b) As in Figure 3a, but with a clipped viewpoint zoomed on the TBsd (in pale magenta to illustrate poor fit). Black arrows indicate unaccounted-for density. (c) As in Figure 3b, with the clipped viewpoint as in panel b of this figure (TBsd now opaque to illustrate good density fit). (d) The KBP-KIF15_MD6S model is shown as opaque ribbons, with kinesin subdomain colouring as in panel a and b and as labelled. KBP is shown as a transparent light grey surface representation. The boxed region indicates that shown in Figure 3c-e. (e) RMSD in Å corresponding to the KIF15_MD6S overlay in panel d, shown on the model of KIF15_MD6S in complex with KBP (grey transparent surface). Parts of the model coloured black are disordered/missing in the KIF15_MD alone crystal structure.

Figure 3–figure supplement 3. Examples of TPR-containing α-solenoid proteins binding α-helical SSE ligands.

(a-d) Comparison of (a) KBP- KIF15_MD6S complex with other TPR-containing α-solenoids shown in blue, and binding peptide motifs shown in magenta or pink for helical and random coil regions respectively; (b) the PINS-INSC complex[30], (c) the CDC16-CDC26 complex[31] and (d) the PscE/PscG-PscF complex[32].

Figure 4–figure supplement 1. Additional KBP α-solenoid edge loops proximal to KIF15_MD6S.

Colouring and representation as in Figure 4. (a) A view showing α-helical pairs αHP1, αHP2, αHP3, αHP8 and αHP9 of KBP and the KIF15_MD6S coloured by subdomain as labelled. (b) Left zoomed region in panel a, with density removed, showing KBP L1, L3, L5 and proximal kinesin elements KL9, KL11 and Kα6. ADP

is coloured in light orchid. (c) Right zoomed region in panel a, with density removed, showing KBP L16 and L18 and proximal KIF15_MD6S elements KNT (kinesin N-terminus), KNL (kinesin neck-linker) and KL12.

Figure 5–figure supplement 1. KBP mutants show similar expression profiles in COS-7 cells.

(a) Representative images of COS-7 cells expressing HA-KBP mutant constructs. Scale bar, 10 µm.

Figure 5–figure supplement 2. Pull-down experiments demonstrate the effect of KBP mutation on the interaction between KIF15 and KIF1A.

(a) Control pull-down experiment with bioGFP-EV, bioGFP-KIF1A_MDC or bioGFP-KIF15_MDC and HA-KBP showing that KBP interacts with KIF1A_MDC and KIF15_MDC, but not with bioGFP-EV. (b, c) Example of pull-down experiments showing the interaction between (b) KIF15_MDC or (c) KIF1A_MDC and mutated KBP constructs in HEK293T cell lysates. Graphs show the quantification of the intensity of the mutated HA-KBP construct in the pull-down fraction over the input fraction divided by the intensity of bioGFP_MDC in the pull-down fraction and normalized to HA-KBP. Data are displayed as mean ± s.e.m. (data from two independent experiments).

Figure 5–figure supplement 3. Kinesin motors show different properties in the peroxisome assay.

(a, b, c) Representative images of peroxisomes in COS-7 cells expressing KIF1A_MDC (a) or KIF15_MDC-FRB (b, c), PEX-mRFP-FKBP and HA (left

1209 panels) with addition of rapalog. Images were thresholded at 10000 (a, b) or 7500 (c)
1210 and peripheral areas of 5 µm (a, b) or 7,5 µm (c) are shown. Scale bars, 10 µm.
1211
1212 **Video 1. KBP undergoes conformational change to relieve clashes when forming**
1213 **a complex with KIF15_MD6S.**
1214 The KBP-alone model was superimposed on the KBP- KIF15_MD6S model using
1215 UCSF Chimera's matchmaker[57]. A conformational morph movie was then generated
1216 in Chimera between the KBP-alone and KIF15 motor domain bound states, with
1217 KIF15_MD6S shown throughout to illustrate the relief of clashes. The N-terminal and
1218 C-terminal subdomains are coloured in olive and gold respectively, as in Figure 2a,b,
1219 while KIF15_MD6S is shown in pale magenta. Distances between identified clashing
1220 atoms when KBP-alone is superimposed onto the KBP- KIF15_MD6S model are
1221 indicated by red linking lines and KBP clashing residues and side chains shown in
1222 cyan. Atoms that were clashing remain coloured while the red lines gradually
1223 disappear as the clashes are relieved by the conformational change. Clashes were
1224 calculated in Chimera using default criteria.
1225
1226 **Video 2. Interaction of KBP with the KIF15 motor domain.**
1227 Model of the KBP- KIF15_MD6S complex (ribbon representation) displayed in
1228 experimental cryo-EM density. The N-terminal (olive) and C-terminal (gold)
1229 subdomains and the linker region (black) are shown in KBP, while the KIF15_MD6S
1230 Switch 1/2 subdomain (Switch 1/2 subdomain) is coloured sienna, the P-loop
1231 subdomain (Kin-PLsd) is coloured light pink and the Kif15_MD tubulin-binding
1232 subdomain (TBsd) is coloured magenta. Semi-transparent density is coloured

regionally as per the fitted model and additional density for the linker loop is shown in semi-transparent black.

Table 1. Cryo-EM reconstruction information and model refinement statistics and model geometry. Data collection, processing and model refinement information for the KBP, KBP- KIF15_MD6S and KIF15_MD6S-MT datasets.

	KBP (EMDB: EMD-11338, PDB: 6ZPG)	**KBP-KIF15_MD6S (EMDB: EMD-11339 , PDB: 6ZPH)**	**KIF15_MD6S-MT (EMDB: EMD-11340, PDB: 6ZPI)**
Data collection and processing			
Pixel size (Å)*	1.055, 1.043 or 1.047	1.047	1.39
Number of micrographs (collected, final)*	9360, 7547	6497, 5138	214,202
Final particle number	258,049 (81,628 of which on graphene oxide)	7,513	12,674
Map resolution (Å)	4.6	6.9	4.5
FSC threshold†	Independent half-map FSC 0.143	Independent half-map FSC 0.143	Independent half-map FSC 0.143
Refinement			
Refinement resolution (Å)	**4.6**	**6.9**	**6**
CC_mask‡	**0.64**	**0.74**	**0.60**
Map sharpening *B*-factor (Å^2)	**-200**	**-495**	**-134**
Model composition			
Nonhydrogen atoms	**3,808**	**6,232**	**9,420**
Protein residues	**610**	**948**	**1185**
Ligands	**0**	**1**	**4**
R.m.s. deviations§			
Bond lengths (Å)	**0.01**	**0.01**	**0.08**
Bond angles (°)	**0.96**	**1.07**	**0.17**
Validation[#]			
MolProbity score	**1.66**	**1.84**	**1.95**
Clashscore	**5.25**	**7.31**	**13.25**
Poor rotamers (%)	**0.5%**	**0.9%**	**0.1%**
Ramachandran plot[#]			
Favored (%)	**94.38**	**93.13**	**95.38**
Allowed (%)	**5.62**	**6.87**	**4.62**
Outliers (%)	**0**	**0**	**0**

*Inclusive of all data collection sessions

†The resolution value at the gold-standard Fourier Shell Correlation (FSC) 0.143 criterion between independently refined half-maps.

‡Cross-correlation provided by Phenix real-space refine[7].

§Root-mean-square deviations of bond lengths or angles in the model.

#As defined by the MolProbity validation server[79].

Table 2. KBP mutants used in this study. The original and mutated amino acid (top) and nucleotide sequences (bottom) are shown for each construct.

Construct	Original sequence	Mutated to
L1	EKEPYK gagaaggaaccatacaag	AAAPAA gcagcagcaccagcagca
L3	TEE acggaggag	AGG gcaggagga
L5	REE agagaagaa	AGA gcaggagca
L10	KISATEDTPEAEGEVPEL aagatctcagccacagaagacactcctgaagctgaaggagaagtgccagagctt	AGAGAGAGPAGAGAGPGG gcaggagcaggagcaggagcaggaccagcaggagcaggagcaggaccaggagga
L12	DGY gatggttat	GGA ggcggcgcg
L14	DLNPQY gacctgaatccacagtat	AAGPAA gcagcaggaccagcagca
L16	NKVFPEHIGEDVL aataaagtattccctgagcatataggggaagatgttctt	AAGAPAGAGAGAA gcagcaggagcaccagcaggagcaggagcaggagcagca
L18	EKHPE gaaaagcatcctgag	AAGPG gcagcaggaccagga
αHP4a	YLAQ tacctagctcaa	ALAA gcactagctgca
αHP4b	Q cag	A gca
αHP5a	TLSQ accttgtcacag	ALSA gcgttgtcagcg

1251

Key Resources Table				
Reagent type (species) or resource	**Designation**	**Source or reference**	**Identifiers**	**Additional information**
gene (Homo Sapiens)	KIAA1279	GenBank	HGNC:23419	
gene (Mus musculus)	KIF1A	GenBank	MGI:108391	
gene (Mus musculus)	KIF15	GenBank	MGI:1098258	
strain, strain background (*Escherichia coli*)	BL21(DE3)	NEB	Cat. #: C2527H	Competent cells
strain, strain background (*Escherichia coli*)	BL21-Gold (DE3)	Agilent	Cat. #: 230130	Competent cells
strain, strain background (*Escherichia coli*)	Rosetta2 (DE3)	Novagen	Cat. #: 71400	Competent cells
cell line (Homo Sapiens)	Human embryonic kidney 239T (HEK293T)	ATCC	CRL-3216 RRID:CVCL_0063	
cell line (Cercopithecus Aethiops)	Cercopithecus aethiops kidney (COS-7)	ATCC	CRL-1651 RRID:CVCL_0224	
peptide, recombinant protein	porcine tubulin (>99% pure)	Cytoskeleton Inc.	Cat. #: T240	
antibody	anti-HA (Mouse monoclonal)	Roche	Cat# 11666606001; RRID:AB_51	IF (1:500)

			4506	
antibody	anti-mouse IgG1, Alexa488 (Goat polyclonal)	Thermo Fisher Scientific	Cat# A-21121, RRID:AB_2535764	IF (1:400)
antibody	anti-HA (Mouse monoclonal)	Biolegend	Cat# 901533; RRID:AB_2801249	WB (1:2000)
antibody	anti-GFP (Rabbit polyclonal)	Abcam	Cat# ab290; RRID:AB_303395	WB (1:10000)
antibody	anti-Rabbit IgG Antibody, IRDye 680LT Conjugated (Goat polyclonal)	LI-COR Biosciences	Cat# 827–11081; RRID:AB_10795015	WB (1:20000)
antibody	anti-Mouse IgG Antibody, IRDye 800CW Conjugated (Goat polyclonal)	LI-COR Biosciences	Cat# 827–08364; RRID:AB_10793856	WB (1:15000)
recombinant DNA reagent	KBP (plasmid)	Kevenaar et al., 2016		Described in Materials and methods
recombinant DNA reagent	KIF1A_MD (plasmid)	Atherton et al., 2014		Described in Materials and methods
recombinant DNA reagent	KIF15_MD (plasmid)	This study		Described in Materials and methods

recombinant DNA reagent	pebioGFP (plasmid)	Van der Vaart et al., 2013	N/A	Described in Materials and methods
recombinant DNA reagent	BirA coding vector (plasmid)	Van der Vaart et al., 2013	N/A	Described in Materials and methods
recombinant DNA reagent	GW1-PEX3-mRFP-FKBP1 (plasmid)	Kevenaar et al., 2016	N/A	Described in Materials and methods
recombinant DNA reagent	βactin-Kif1A_MDC-FRB (plasmid)	Kevenaar et al., 2016	N/A	Described in Materials and methods
recombinant DNA reagent	βactin-Kif15_MDC-FRB (plasmid)	This study	N/A	Described in Materials and methods
recombinant DNA reagent	pebioGFP-Kif1A_MDC (plasmid)	This study	N/A	Described in Materials and methods
recombinant DNA reagent	pebioGFP-Kif15_MDC (plasmid)	This study	N/A	Described in Materials and methods
recombinant DNA reagent	pGW1-HA-KBP (plasmid)	This study	N/A	Described in Materials and methods
recombinant DNA reagent	pGW1-HA-KBP_L1 (plasmid)	This study	N/A	Described in Materials and methods
recombinant DNA reagent	pGW1-HA-KBP_L3 (plasmid)	This study	N/A	Described in Materials and methods

recombinant DNA reagent	pGW1-HA-KBP_L5 (plasmid)	This study	N/A	Described in Materials and methods
recombinant DNA reagent	pGW1-HA-KBP_L10 (plasmid)	This study	N/A	Described in Materials and methods
recombinant DNA reagent	pGW1-HA-KBP_L12 (plasmid)	This study	N/A	Described in Materials and methods
recombinant DNA reagent	pGW1-HA-KBP_L14 (plasmid)	This study	N/A	Described in Materials and methods
recombinant DNA reagent	pGW1-HA-KBP_L16 (plasmid)	This study	N/A	Described in Materials and methods
recombinant DNA reagent	pGW1-HA-KBP_L18 (plasmid)	This study	N/A	Described in Materials and methods
recombinant DNA reagent	pGW1-HA-KBP_L10+L12 (plasmid)	This study	N/A	Described in Materials and methods
recombinant DNA reagent	pGW1-HA-KBP_L10+L14 (plasmid)	This study	N/A	Described in Materials and methods
recombinant DNA reagent	pGW1-HA-KBP_L12+L14 (plasmid)	This study	N/A	Described in Materials and methods
recombinant DNA reagent	pGW1-HA-KBP_αHP4a (plasmid)	This study	N/A	Described in Materials and methods

recombinant DNA reagent	pGW1-HA-KBP_αHP4b (plasmid)	This study	N/A	Described in Materials and methods
recombinant DNA reagent	pGW1-HA-KBP_αHP5a (plasmid)	This study	N/A	Described in Materials and methods
sequence-based reagent	KBP_fwd	This study	PCR primer for KBP mutants	TATTATTA TGGCGCGC CAGGATCC CCGGAATT CGGCACGA GGGAGGC CGCTATGG CGAACGTT CCGTGGGC A
sequence-based reagent	KBP_rev	This study	PCR primer for KBP mutants	CTCGTCGA CTCCTAAT CCTTAAGT CAGGGCCA TCTT
sequence-based reagent	KBP_L1_fwd	This study	PCR primer for KBP_L1	CTGCATAA AAATCCGG CAGCAGCA CCAGCAGC ATCCAAAT ACAGCGCC
sequence-based reagent	KBP_L1_rev	This study	PCR primer for KBP_L1	GGCGCTGT ATTTGGAT GCTGCTGG TGCTGCTG CCGGATTT TTATGCAG
sequence-based reagent	KBP_L3_fwd	This study	PCR primer for KBP_L3	TGAACCAC ATCGACGC AGGAGGA CTGTCGGC GGGGGA
sequence-based reagent	KBP_L3_rev	This study	PCR primer for KBP_L3	TCCCCCGC CGACAGTC CTCCTGCG TCGATGTG

				GTTCA
sequence-based reagent	KBP_L5_fwd	This study	PCR primer for KBP_L5	ATCTTGTG GTCTGAAG CAGGAGC AATTGAAA CTGCACAG
sequence-based reagent	KBP_L5_rev	This study	PCR primer for KBP_L5	CTGTGCAG TTTCAATT GCTCCTGC TTCAGACC ACAAGAT
sequence-based reagent	KBP_L10_fwd	This study	PCR primer for KBP_L10	TTTGGTCA AACTGGAG CAGGAGC AGGAGCA GGAGCAG GACCAGCA GGAGCAG GAGCAGG ACCAGGA GGATATCA TCAAAGAA A
sequence-based reagent	KBP_L10_rev	This study	PCR primer for KBP_L10	TTTCTTTG ATGATATC CTCCTGGT CCTGCTCC TGCTCCTG CTGGTCCT GCTCCTGC TCCTGCTC CTGCTCCA GTTTGACC AAA
sequence-based reagent	KBP_L12_fwd	This study	PCR primer for KBP_L12	GAGTTCTT TCAGATTG GCGGCGCG GTCACTGA CCATATT

sequence-based reagent	KBP_L12_rev	This study	PCR primer for KBP_L12	AATATGGTCAGTGACCGCGCCGCCAATCTGAAAGAACTC
sequence-based reagent	KBP_L14_fwd	This study	PCR primer for KBP_L14	TAGAGCCCCTAACTGTAGCAGCAGGACCAGCAGCATATCTGTTGGTCAAC
sequence-based reagent	KBP_L14_rev	This study	PCR primer for KBP_L14	GTTGACCAACAGATATGCTGCTGGTCCTGCTGCTACAGTTAGGGGCTCTA
sequence-based reagent	KBP_L16_fwd	This study	PCR primer for KBP_L16	TCCCTGAGAGACCCAGCAGCAGGAGCACCAGCAGGAGCAGGAGCAGGAGCACGCCCTGCCATGTTA
sequence-based reagent	KBP_L16_rev	This study	PCR primer for KBP_L16	TAACATGGCAGGGCGTGCTGCTCCTGCTCCTGCTCTCCTGCTGGTGCTCCTGCTGCTGGGTCTCTCAGGGA
sequence-based reagent	KBP_L18_fwd	This study	PCR primer for KBP_L18	ATTGTTGATTACTGTGCAGCAGGACCAGGAGCCGCCCAGGAAATA

sequence-based reagent	KBP_L18_rev	This study	PCR primer for KBP_L18	TATTTCCT GGGCGGCT CCTGGTCC TGCTGCAC AGTAATCA ACAAT
sequence-based reagent	KBP_HP4a_fwd	This study	PCR primer for KBP_L HP4a	ACTCATAA CCTATATG CACTAGCT GCAGTCTA CCAGCATC TG
sequence-based reagent	KBP_L HP4a _rev	This study	PCR primer for KBP_ HP4a	CAGATGCT GGTAGACT GCAGCTAG TGCATATA GGTTATGA GT
sequence-based reagent	KBP_HP4b_fwd	This study	PCR primer for KBP_L HP4b	AGTACACT AAAACGC GCACTTGA GCACAATG CC
sequence-based reagent	KBP_L HP4b _rev	This study	PCR primer for KBP_ HP4b	GGCATTGTG CTCAAGTGC GCGTTTTAGT GTACT
sequence-based reagent	KBP_HP5a_fwd	This study	PCR primer for KBP_L HP5a	GCTATCAA TGCTGCTG CGTTGTCA GCGTTTTA CATCAATA AG
sequence-based reagent	KBP_ HP5a _rev	This study	PCR primer for KBP_ HP5a	CTTATTGA TGTAAAAC GCTGACAA CGCAGCAG CATTGATA GC
sequence-based reagent	KIF15_FRB_ fwd	This study	PCR primer for KIF15-FRB	AAGCTTGC CACCATGG GCGCGCCT GCCACCAT GGCTCCTG

				GCTGCAAATCT
sequence-based reagent	KIF15_FRB_rev	This study	PCR primer for KIF15-FRB	AGAGGATTCTAGAAGCAGGCGCGCCAGCGTAGTCTGGGACGTCGTATGGGTAGAATTCTCCTGGTGTCAGCTGCCCAGA
sequence-based reagent	bioGFPKIF15 _fwd	This study	PCR primer for bioGFPKIF15	AGCTCAAGCTTCGAATTGGGCGCGCCAGCCACCATGGCTCCTGGCTGCAAATCT
sequence-based reagent	bioGFPKIF15_rev	This study	PCR primer for bioGFPKIF15	GAATTCGATATCCTGCAGGTCGACTCCAGATCCTCATCCTGGTGTCAGCTGCCCAGA
sequence-based reagent	bioGFPKIF1A _fwd	This study	PCR primer for bioGFPKIF1A	TATTATAATGGCGCGCCAGCCACCGCCGGGGCCTCTGTGAAGGT
sequence-based reagent	bioGFPKIF1A_rev	This study	PCR primer for bioGFPKIF1A	CTCGTCGACTCCTCCTCCTCATTTGGGAGAAAACACACCCAA
commercial assay or kit	EnzChek™ Phosphate Assay Kit	Invitrogen™	E6646	

chemical compound, drug	AP21967	TaKaRa	Cat# 635057	1 µM
chemical compound, drug	PEI	PolySciences	Cat# 24765–2	
chemical compound, drug	Fugene	Promega	Cat# E2692	
software, algorithm	ImageJ	NIH	https://imagej.nih.gov/ij/; RRID:SCR_003070	
software, algorithm	RELION	Zivanov et al., 2018	n/a	
software, algorithm	CryoSparc2	Punjani et al., 2017	n/a	
software, algorithm	CisTEM	Grant et al., 2018	n/a	
software, algorithm	MiRP	Cook et al., 2020	n/a	Protocol implemented in RELION

1252

Figure 1

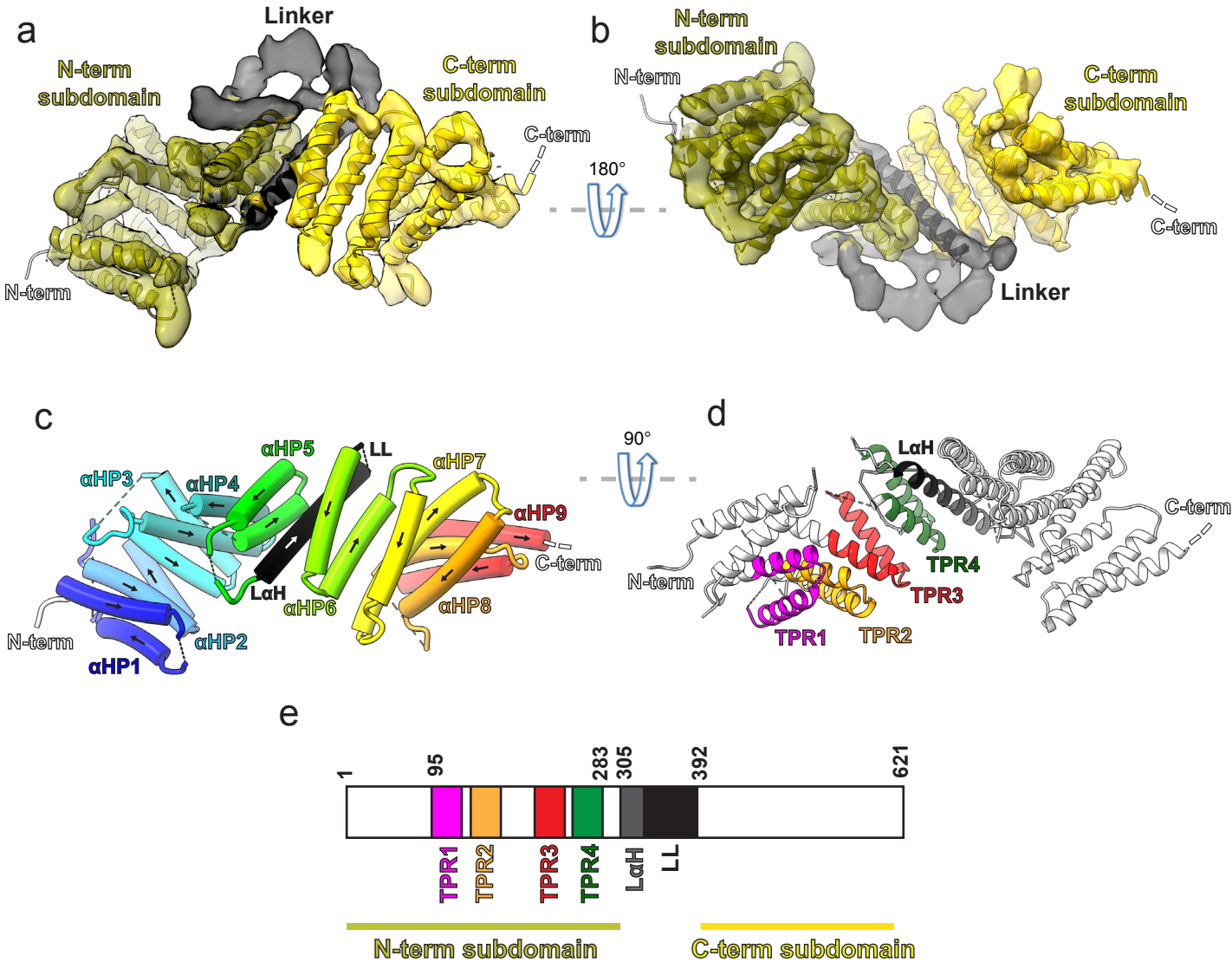
a
Linker
N-term subdomain
C-term subdomain
C-term
N-term
b
N-term subdomain
N-term
C-term subdomain
180°
C-term
Linker
c
αHP5
LL
αHP7
αHP3
αHP4
αHP9
C-term
LαH
αHP6
αHP8
N-term
αHP2
αHP1
d
90°
LαH
C-term
N-term
TPR4
TPR3
TPR1
TPR2
e
1
95
283
305
392
621
TPR1
TPR2
TPR3
TPR4
LαH
LL
N-term subdomain
C-term subdomain

Figure 1-figure supplement 1

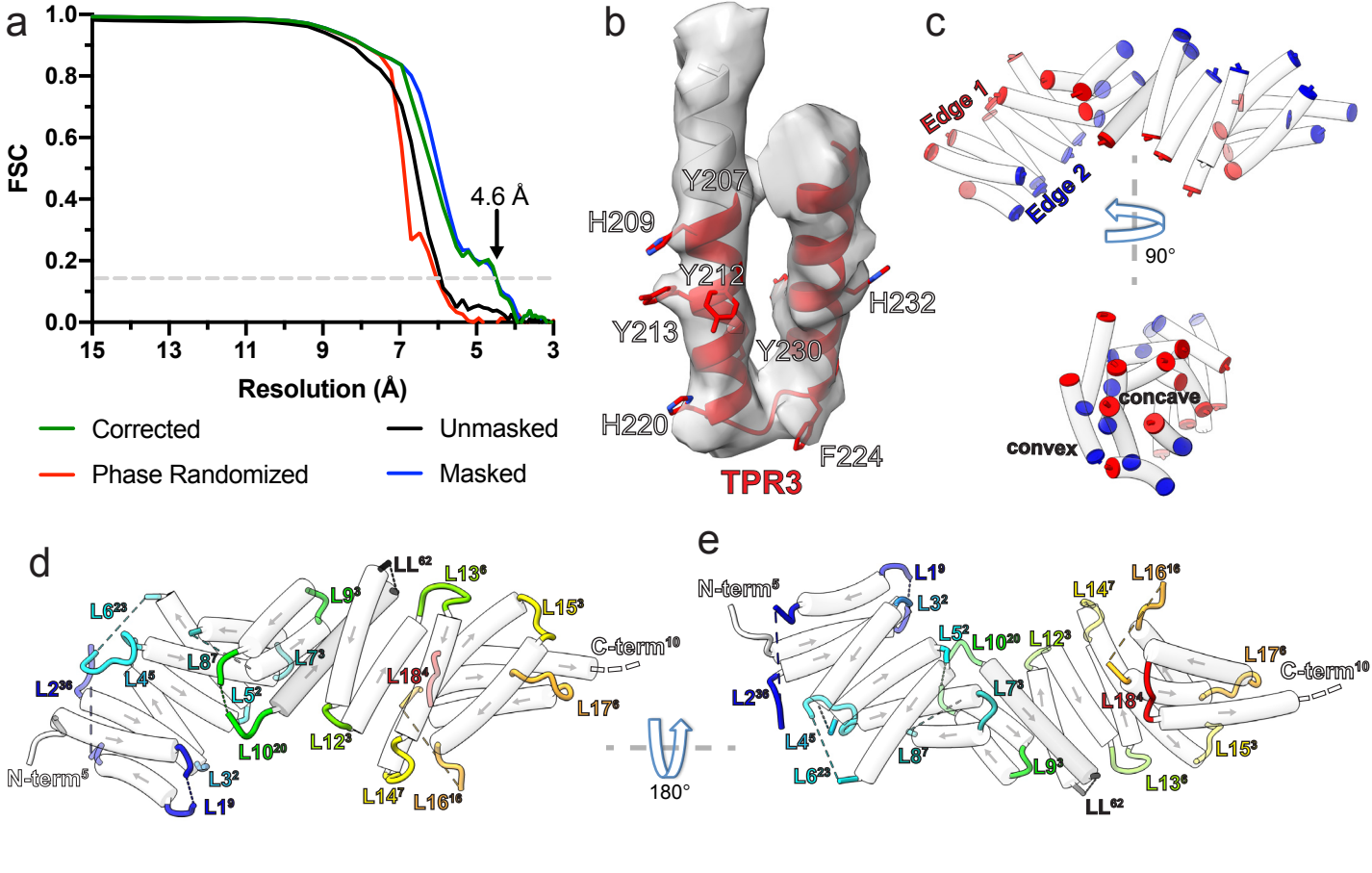

Figure 1-figure supplement 2

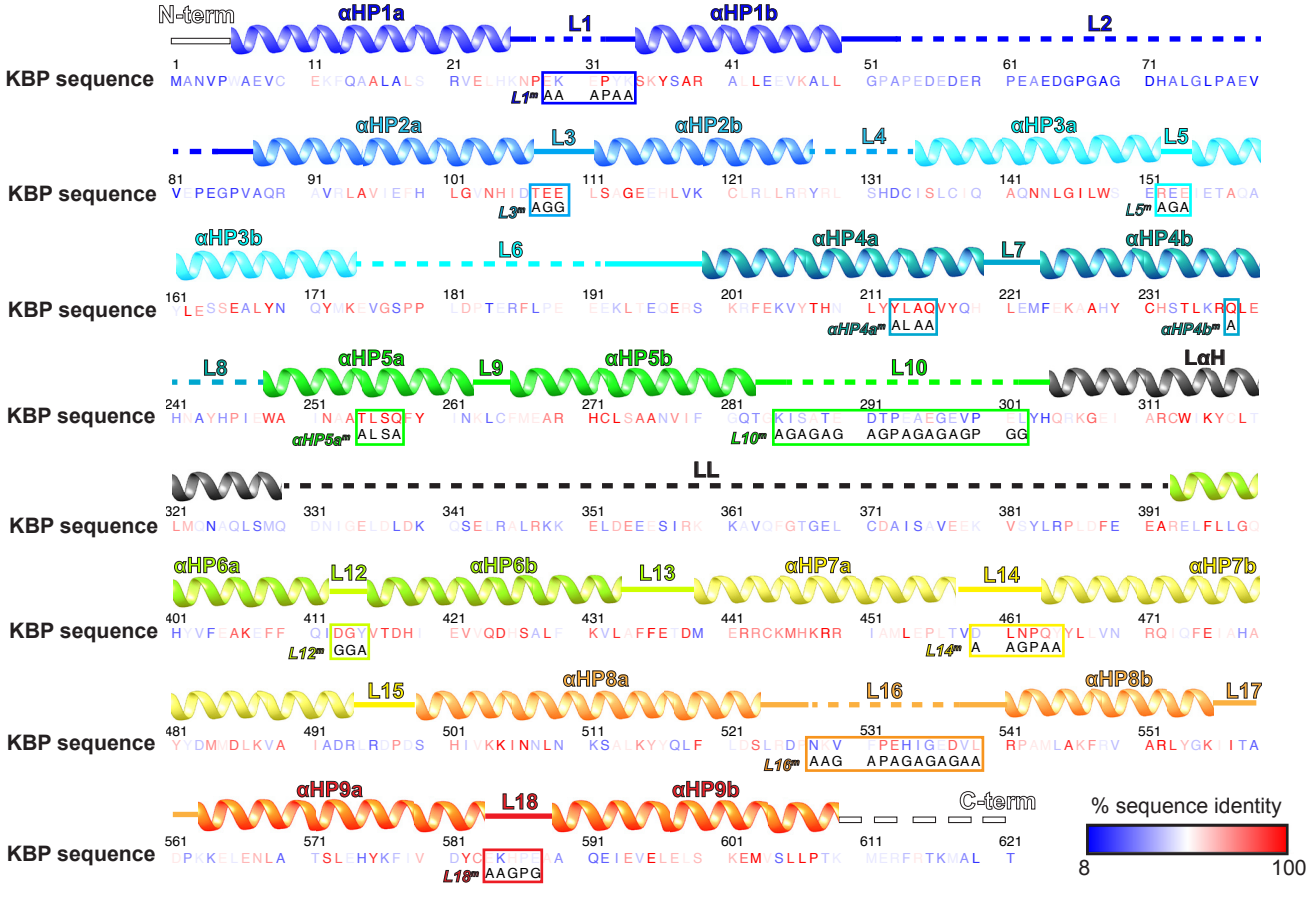

Figure 1-figure supplement 3

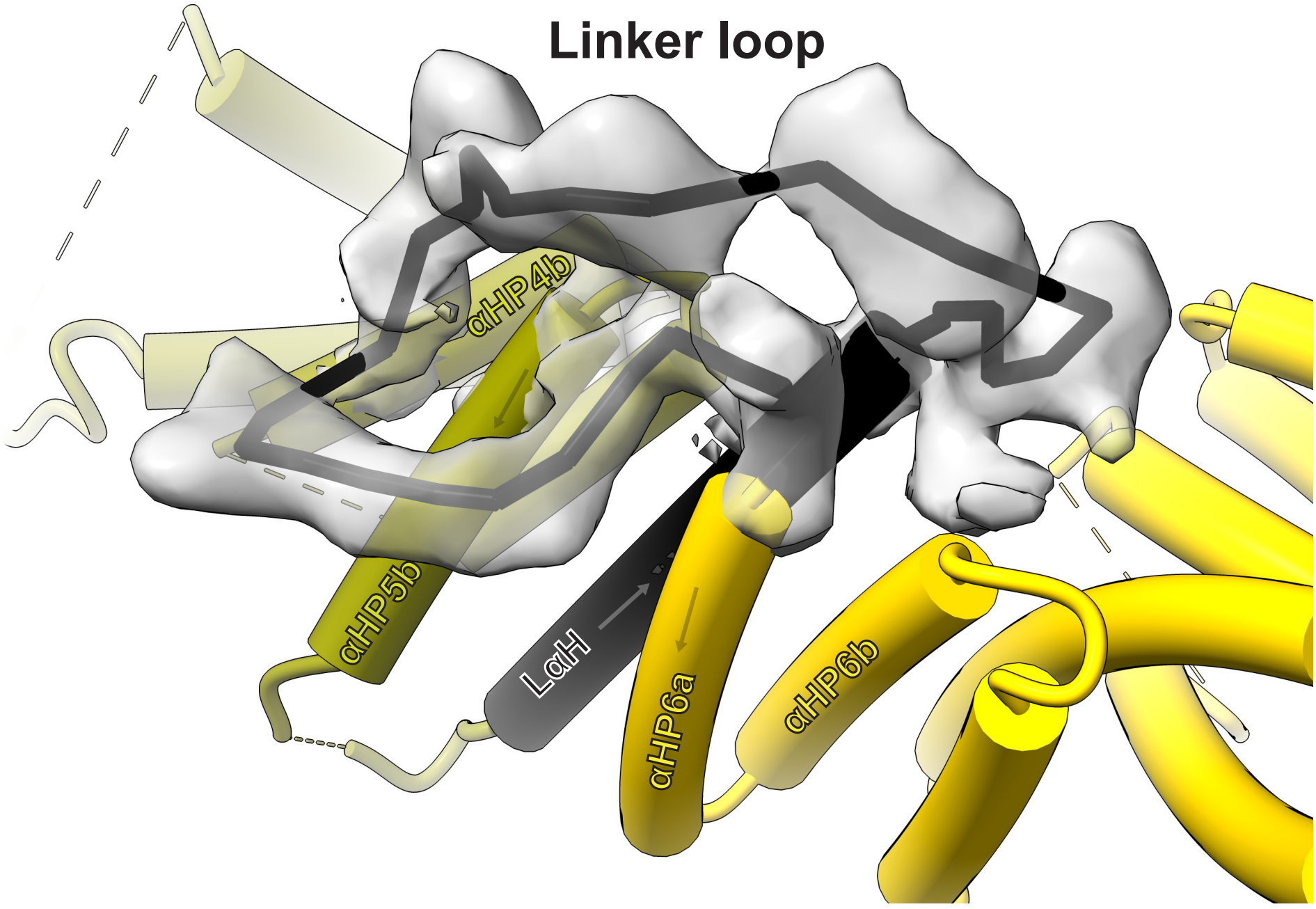

Figure 2

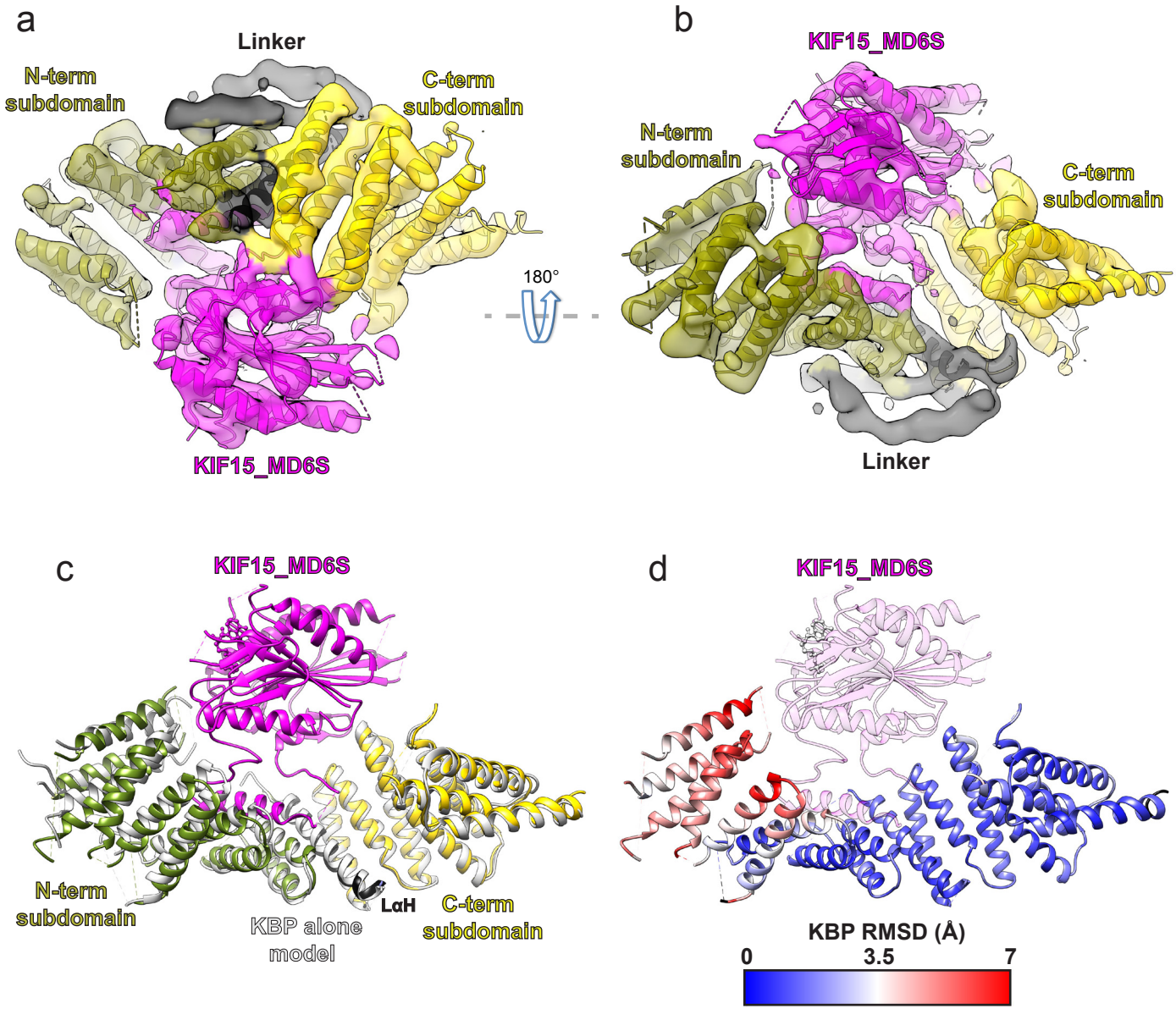
a
Linker
N-term subdomain
C-term subdomain
KIF15_MD6S
180°
b
KIF15_MD6S
N-term subdomain
C-term subdomain
Linker
c
KIF15_MD6S
N-term subdomain
KBP alone model
LαH
C-term subdomain
d
KIF15_MD6S
KBP RMSD (Å)
0
3.5
7

Figure 2-figure supplement 1

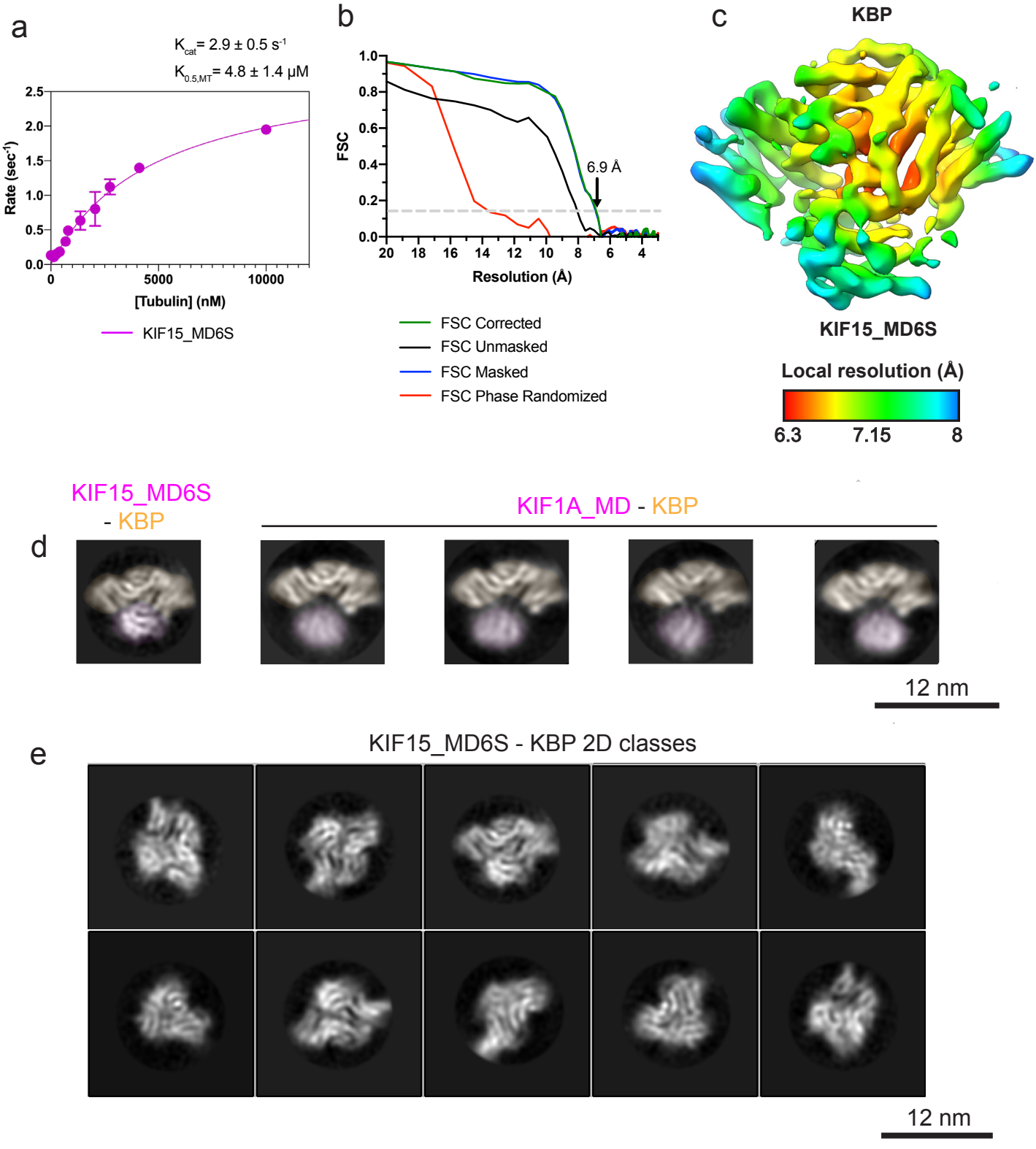

Figure 3

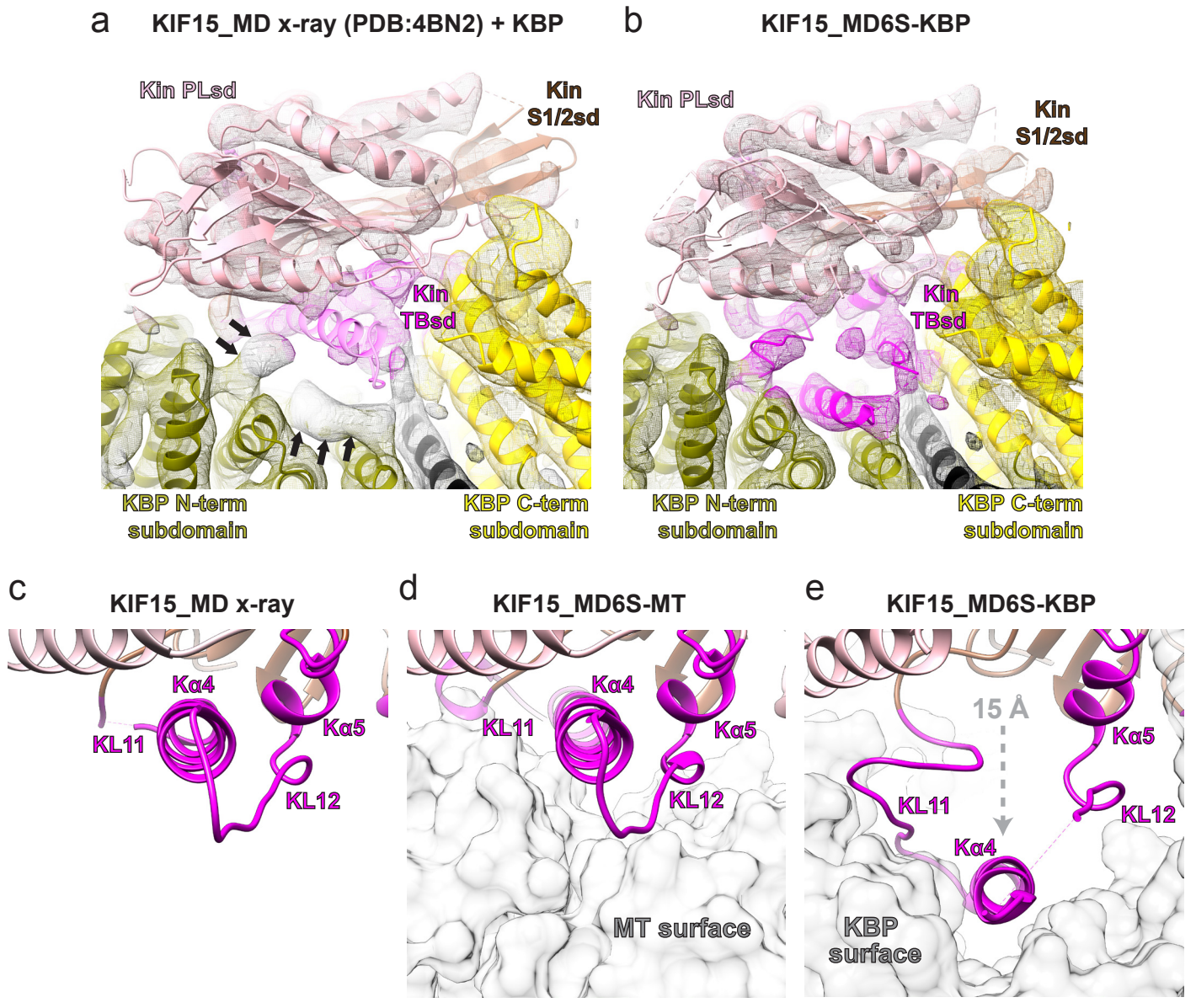
a
KIF15_MD x-ray (PDB:4BN2) + KBP
Kin PLsd
Kin S1/2sd
Kin TBsd
KBP N-term subdomain
KBP C-term subdomain
b
KIF15_MD6S-KBP
Kin PLsd
Kin S1/2sd
Kin TBsd
KBP N-term subdomain
KBP C-term subdomain
c
KIF15_MD x-ray
Kα4
Kα5
KL11
KL12
d
KIF15_MD6S-MT
Kα4
Kα5
KL11
KL12
MT surface
e
KIF15_MD6S-KBP
15 Å
Kα5
KL11
KL12
Kα4
KBP surface

Figure 3-figure supplement 1

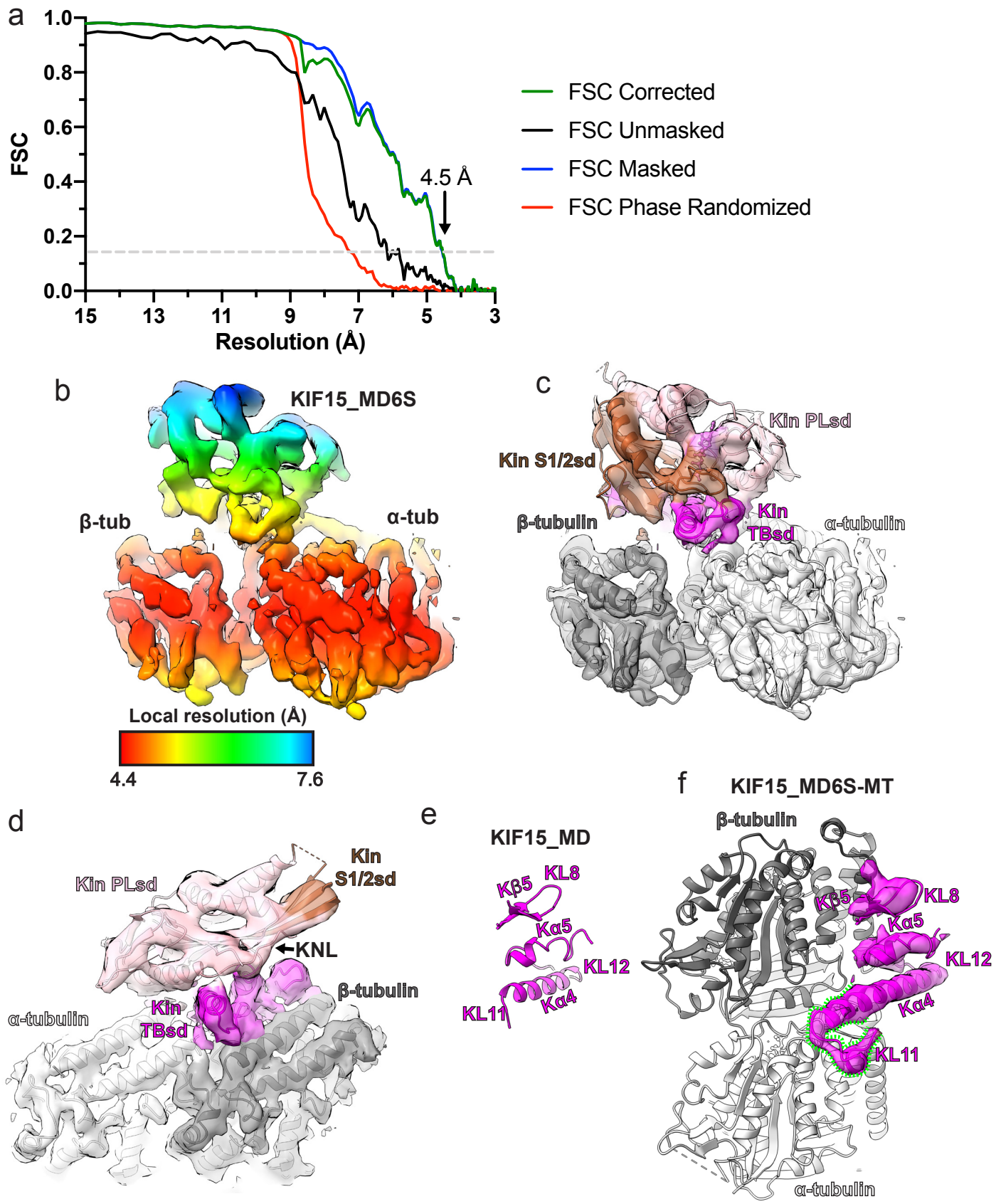

Figure 3-figure supplement 2

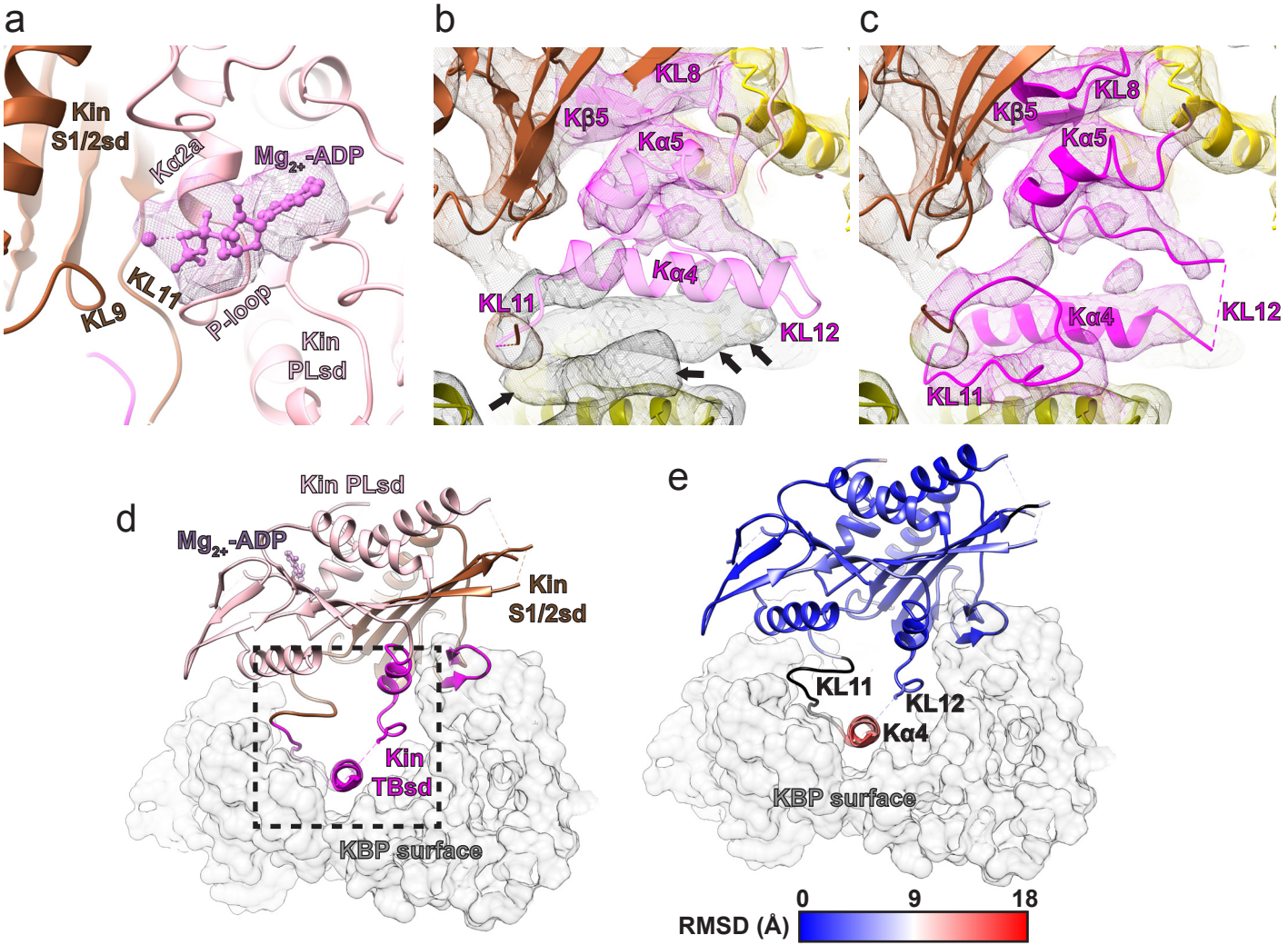

Figure 3-figure supplement 3

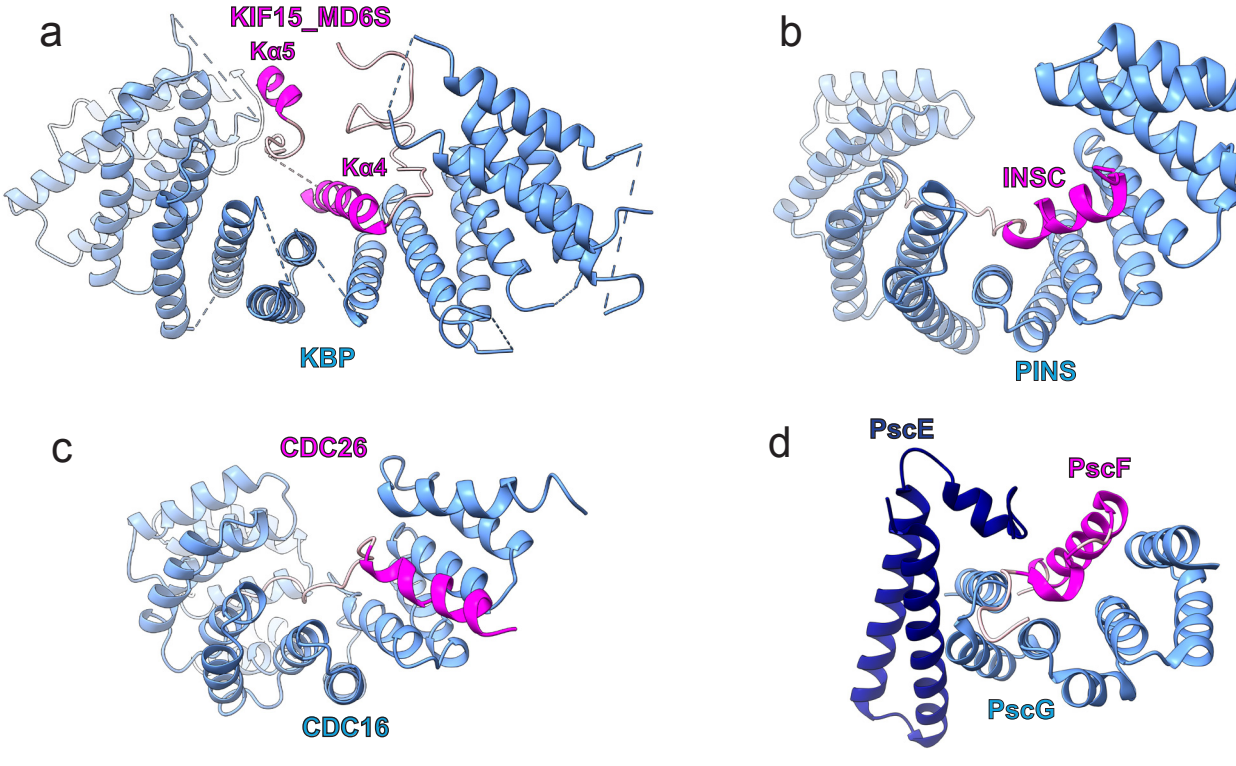

Figure 4

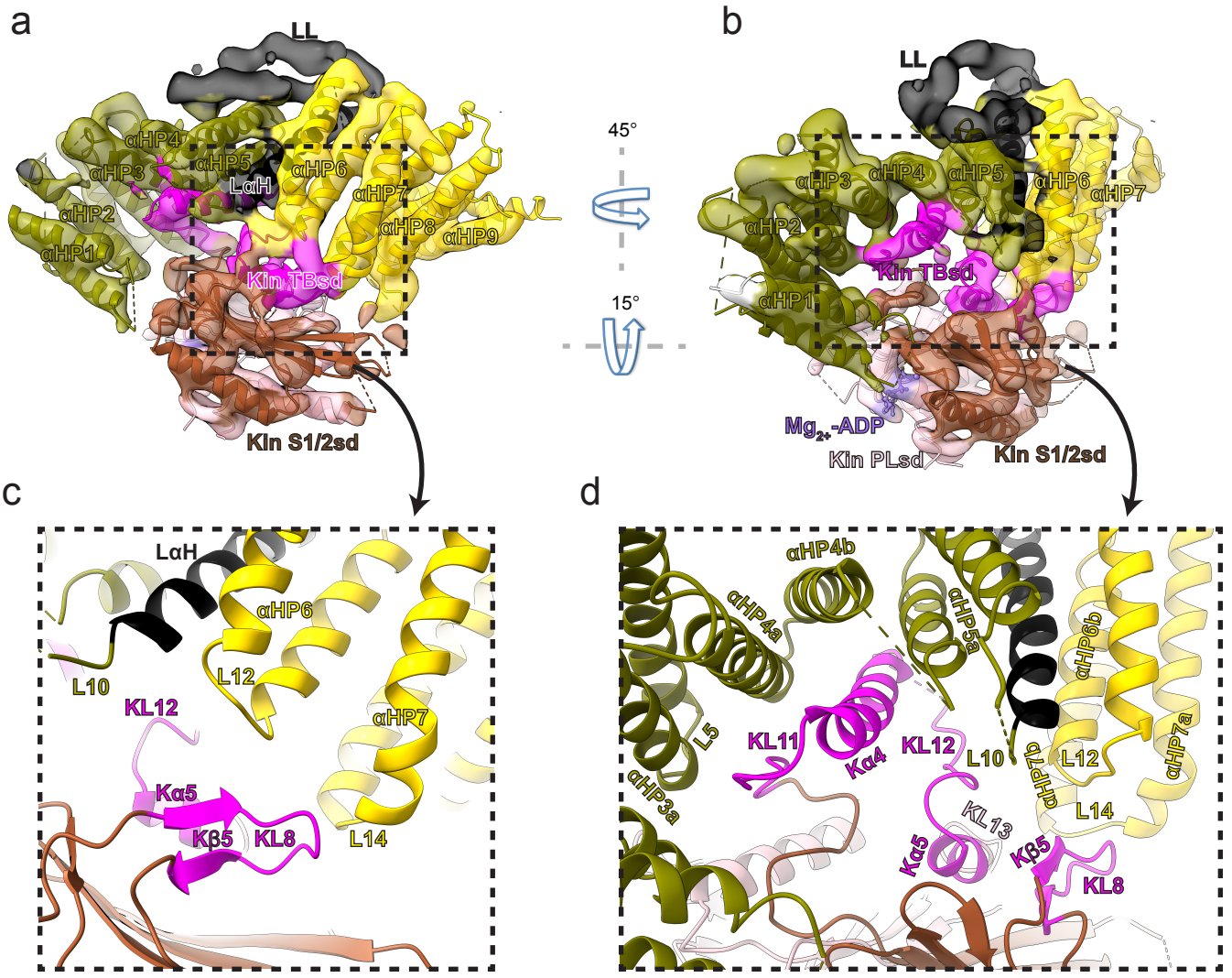
a
LL
αHP4
αHP3
αHP5
LαH
αHP6
αHP7
αHP2
αHP8
αHP9
αHP1
Kin TBsd
Kin S1/2sd
45°
15°
b
LL
αHP3
αHP4
αHP5
αHP6
αHP7
αHP2
αHP1
Kin TBsd
Mg2+-ADP
Kin PLsd
Kin S1/2sd
c
LαH
αHP6
L10
L12
KL12
αHP7
Kα5
Kβ5
KL8
L14
d
αHP4b
αHP4a
αHP5a
αHP6b
αHP7b
αHP7a
L5
KL11
Kα4
KL12
L10
L12
αHP3a
KL13
L14
Kα5
Kβ5
KL8

Figure 4-figure supplement 1

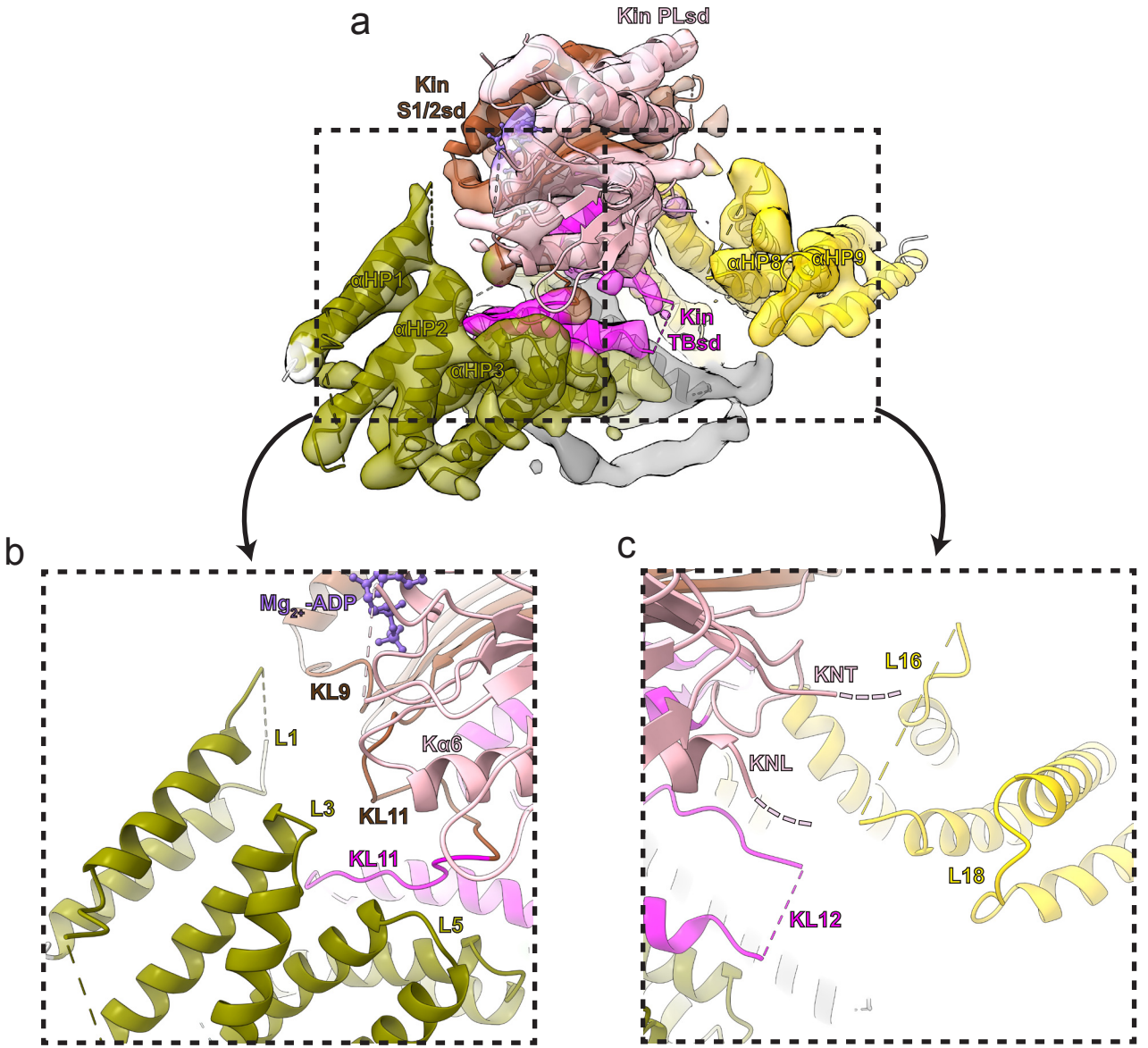

Figure 5

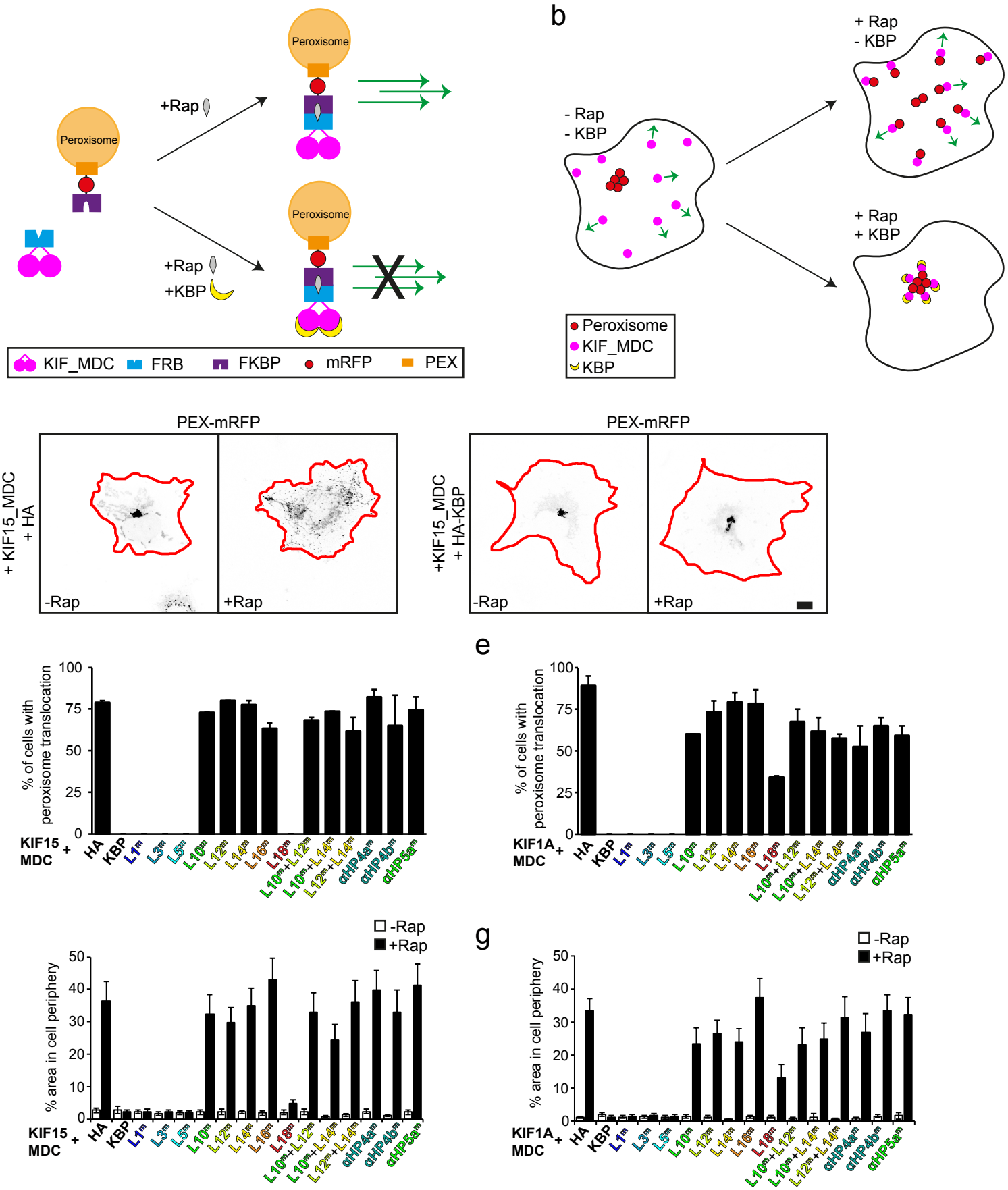
a
Peroxisome
+Rap
Peroxisome
+Rap
+KBP
Peroxisome
KIF_MDC
FRB
FKBP
mRFP
PEX
b
- Rap
- KBP
+ Rap
- KBP
+ Rap
+ KBP
Peroxisome
KIF_MDC
KBP
c
PEX-mRFP
+ KIF15_MDC
+ HA
-Rap
+Rap
PEX-mRFP
+KIF15_MDC
+ HA-KBP
-Rap
+Rap
d
% of cells with peroxisome translocation
100
75
50
25
0
KIF15 MDC +
HA
KBP
L1m
L3m
L5m
L10m
L12m
L14m
L16m
L18m
L10m+L12m
L10m+L14m
L12m+L14m
αHP4am
αHP4bm
αHP5am
e
% of cells with peroxisome translocation
100
75
50
25
0
KIF1A MDC +
HA
KBP
L1m
L3m
L5m
L10m
L12m
L14m
L16m
L18m
L10m+L12m
L10m+L14m
L12m+L14m
αHP4am
αHP4bm
αHP5am
f
-Rap
+Rap
% area in cell periphery
50
40
30
20
10
0
KIF15 MDC +
HA
KBP
L1m
L3m
L5m
L10m
L12m
L14m
L16m
L18m
L10m+L12m
L10m+L14m
L12m+L14m
αHP4am
αHP4bm
αHP5am
g
-Rap
+Rap
% area in cell periphery
50
40
30
20
10
0
KIF1A MDC +
HA
KBP
L1m
L3m
L5m
L10m
L12m
L14m
L16m
L18m
L10m+L12m
L10m+L14m
L12m+L14m
αHP4am
αHP4bm
αHP5am

Figure 5-figure supplement 1

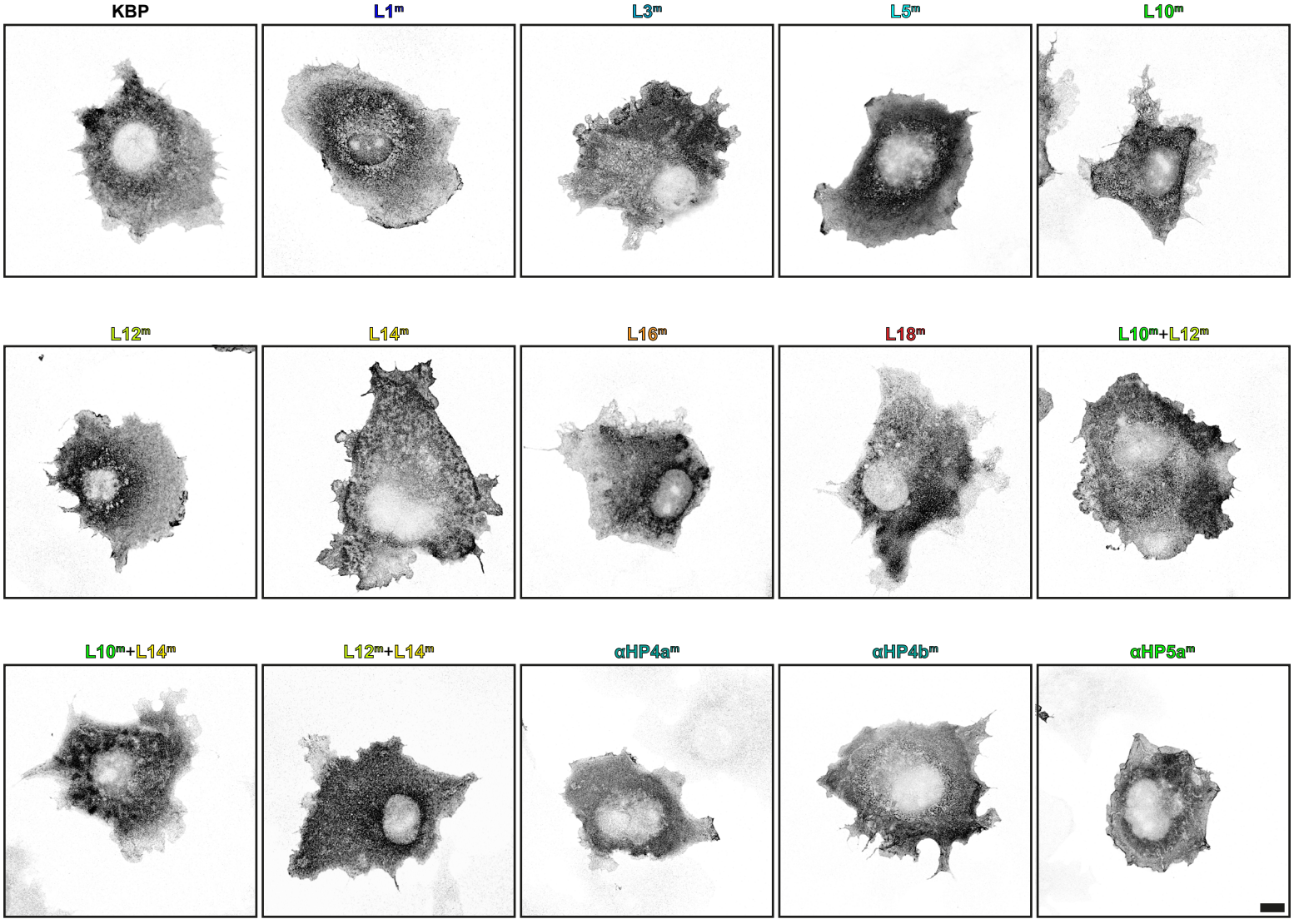

Figure 5-figure supplement 2

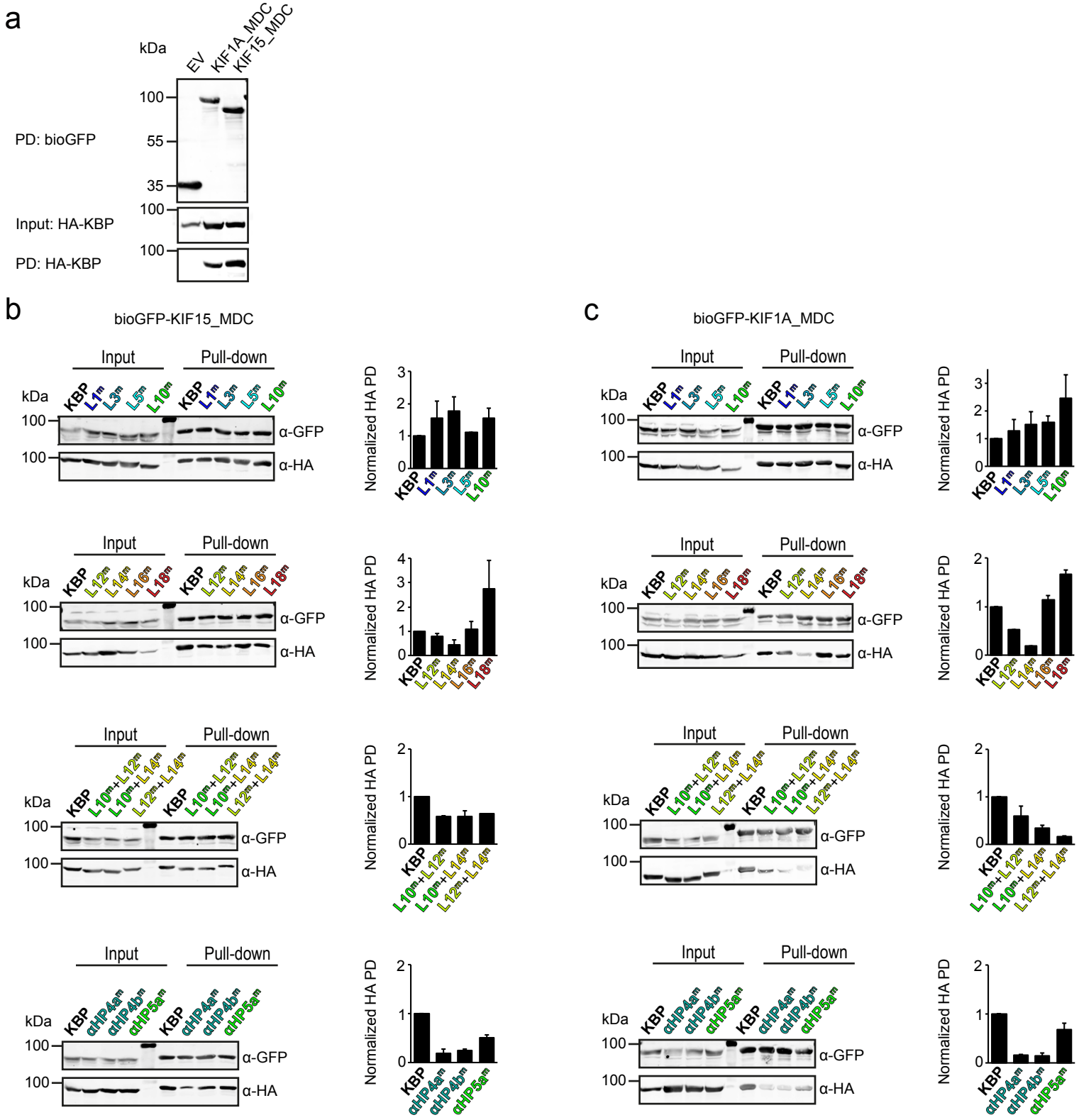

Figure 5-figure supplement 3

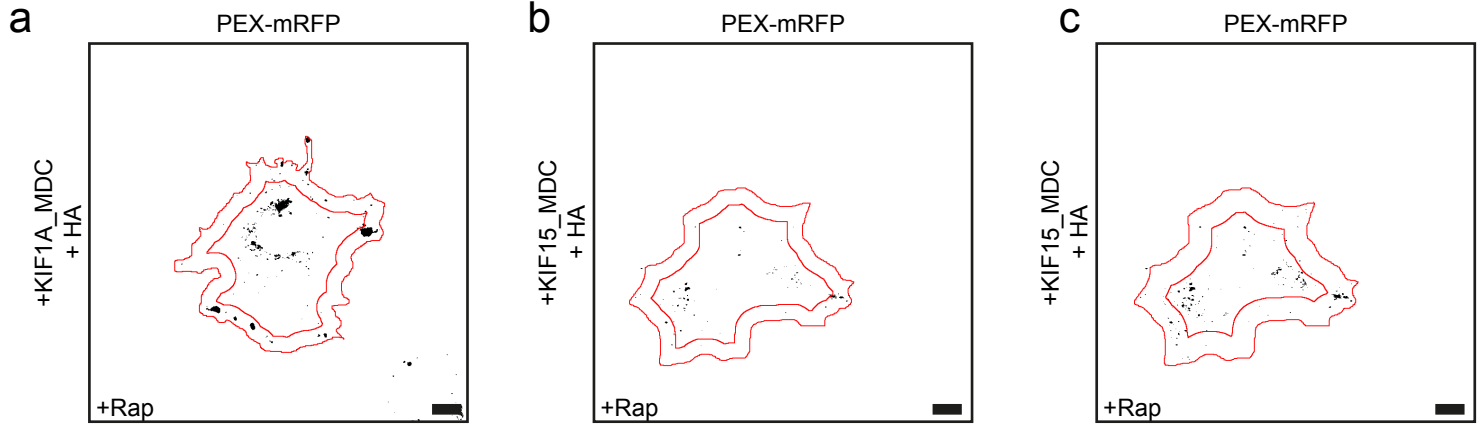

Figure 6

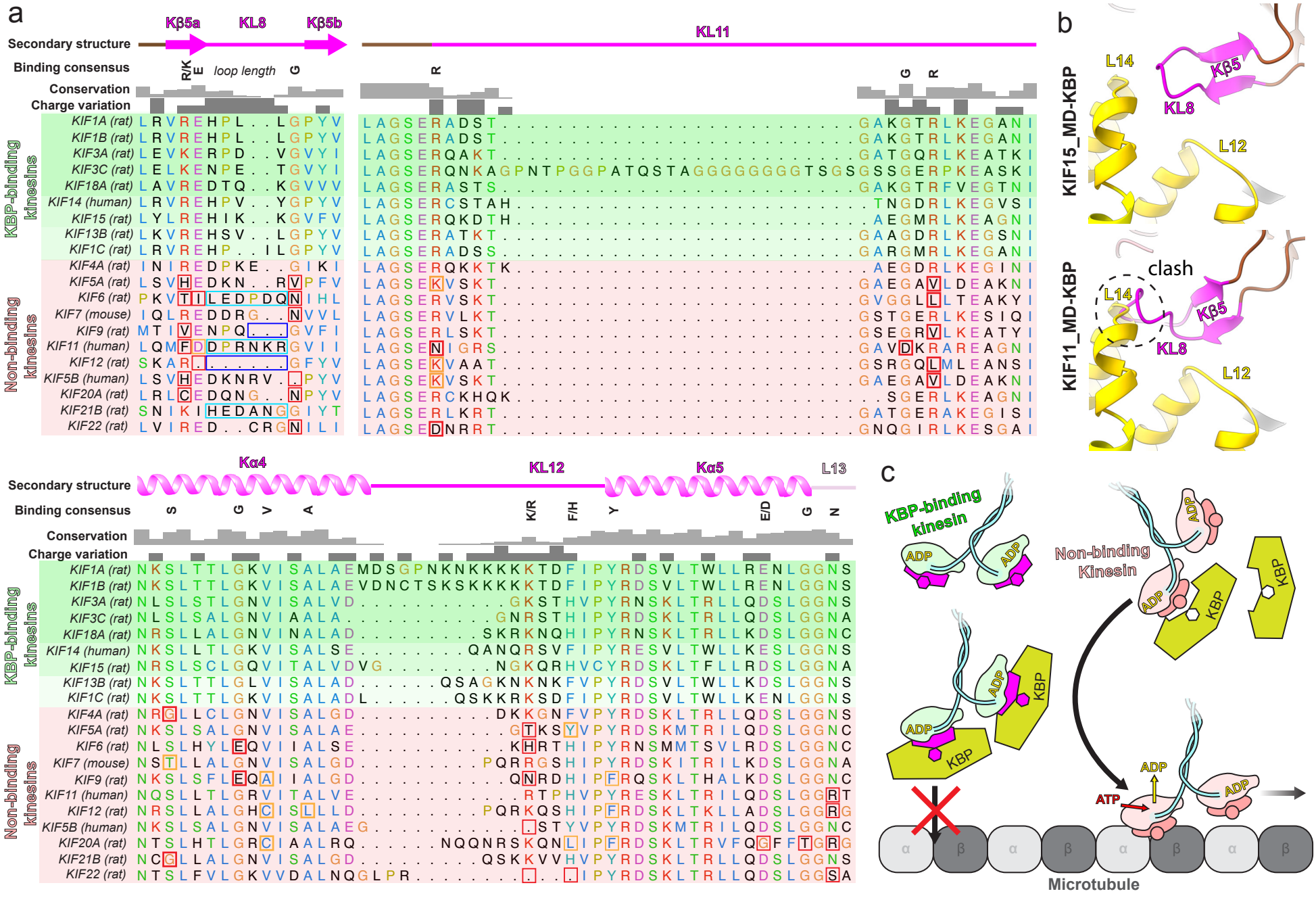
a
Kβ5a
KL8
Kβ5b
KL11
Secondary structure
Binding consensus
R/K
E
loop length
G
R
G
R
Conservation
Charge variation
KBP-binding kinesins
KIF1A (rat) LRVREHPL..LGPYV LAGSERADST.....GAKGTRLKEGANI
KIF1B (rat) LRVREHPL..LGPYV LAGSERADST.....GAKGTRLKEGANI
KIF3A (rat) LEVKERPD..VGVYI LAGSERQAKT.....GATGQRLKEATKI
KIF3C (rat) LELKENPE..TGVYI LAGSERQNKAGPNTPGGPATQSTAGGGGGGGGTSGSGSSGERPKEASKI
KIF18A (rat) LAVREDTQ..KGVVV LAGSERASTS.....GAKGTRFVEGTNI
KIF14 (human) LRVREHPV..YGPYV LAGSERCSTAH.....TNGDRLKEGVSI
KIF15 (rat) LYLREHIK..KGVFV LAGSERQKDTH.....AEGMRLKEAGNI
KIF13B (rat) LKVREHSV..LGPYV LAGSERATKT.....GAAGDRLKEGSNI
KIF1C (rat) LRVREHP..ILGPYV LAGSERADSS.....GARGMRLKEGANI
Non-binding kinesins
KIF4A (rat) INIREDPKE..GIKI LAGSERQKKTK.....AEGDRLKEGINI
KIF5A (rat) LSVHEDKN..RVPFV LAGSEKVSKT.....GAEGAVLDEAKNI
KIF6 (rat) PKVTILEDPDQNIHL LAGSERVSKT.....GVGGLLLTEAKYI
KIF7 (mouse) IQLREDDRG..NVVL LAGSERVLKT.....GSTGERLKESIQI
KIF9 (rat) MTIVENPQ....GVFI LAGSERLSKT.....GSEGRVLKEATYI
KIF11 (human) LQMFDDPRNKRGVII LAGSENIGRS.....GAVDKRAREAGNI
KIF12 (rat) SKAR.....GFYV LAGSEKVAAT.....GSRGQLMLEANSI
KIF5B (human) LSVHEDKNRV..PYV LAGSEKVSKT.....GAEGAVLDEAKNI
KIF20A (rat) LRLCEDQNG..NPYV LAGSERCKHQK.....SGERLKEAGNI
KIF21B (rat) SNIKIHEDANGGIYT LAGSERLKRT.....GATGERAKEGISI
KIF22 (rat) LVIRED..CRGNILI LAGSEDNRRT.....GNQGIRLKESGAI
b
KIF15_MD-KBP
L14
Kβ5
KL8
L12
KIF11_MD-KBP
clash
L14
Kβ5
KL8
L12
Kα4
KL12
Kα5
L13
Secondary structure
Binding consensus
S
G
V
A
K/R
F/H
Y
E/D
G
N
Conservation
Charge variation
KBP-binding kinesins
KIF1A (rat) NKSLTTLGKVISALAEMDSGPNKNKKKKKTDFIPYRDSVLTWLLRENLGGNS
KIF1B (rat) NKSLTTLGKVISALAEVDNCTSKSKKKKKTDFIPYRDSVLTWLLRENLGGNS
KIF3A (rat) NLSLSTLGNVISALVD.....GKSTHVPYRNSKLTRLLQDSLGGNS
KIF3C (rat) NLSLSALGNVIAALA.....GNRSTHIPYRDSKLTRLLQDSLGGNA
KIF18A (rat) NRSLLALGNVINALAD.....SKRKNQHIPYRNSKLTRLLKDSLGGNC
KIF14 (human) NKSLLTLGKVISALSE.....QANQRSVFIPYRESVLTWLLKESLGGNS
KIF15 (rat) NRSLSCLGQVITALVDVG.....NGKQRHVCYRDSKLTFLLRDSLGGNA
KIF13B (rat) NKSLTTLGLVISALAD.....QSAGKNKNKFVPYRDSVLTWLLKDSLGGNS
KIF1C (rat) NKSLTTLGKVISALADL.....QSKKRKSDFIPYRDSVLTWLLKENLGGNS
Non-binding kinesins
KIF4A (rat) NRGLCLGNVISALGD.....DKKGNFVPYRDSKLTRLLQDSLGGNS
KIF5A (rat) NKSLSALGNVISALAE.....GTKSYVPYRDSKMTRILQDSLGGNC
KIF6 (rat) NLSLHYLEQVIIALSE.....KHRTHIPYRNSMMTSVLRDSLGGNC
KIF7 (mouse) NSTLLALGNVISALGD.....PQRRGSHIPYRDSKITRILKDSLGGNA
KIF9 (rat) NKSLSFLEQAIIALGD.....QNRDHIPFRQSKLTHALKDSLGGNC
KIF11 (human) NQSLLTLGRVITALVE.....RTPHVPYRESKLTRILQDSLGGRT
KIF12 (rat) NRSLLALGHCISLLLD.....PQRKQSHIPFRDSKLTKLLADSLGGRG
KIF5B (human) NKSLSALGNVISALAEG.....STYVPYRDSKMTRILQDSLGGNC
KIF20A (rat) NTSLHTLGRCIAALRQ.....NQQNRSKQNLIPFRDSKLTRVFQGFFTGRG
KIF21B (rat) NCGLLALGNVISALGD.....QSKKVVHVPYRDSKLTRLLQDSLGGNS
KIF22 (rat) NTSLFVLGKVVDALNQGLPR.....IPYRDSKLTRLLQDSLGGSA
c
KBP-binding kinesin
ADP
ADP
Non-binding Kinesin
ADP
ADP
KBP
KBP
ADP
ADP
KBP
KBP
ATP
ADP
ADP
α
β
α
β
α
β
α
β
Microtubule